Characterization of Cu-5Fe (wt. %) fabricated by powder consolidation using high-pressure torsion

Amar Djemli[1,2], Hiba Azzeddine[3,*], Piotr Bazarnik[4], Foudil Sahnoune[1], Yi Huang[5], Thierry Baudin[6], François Brisset[6], Megumi Kawasaki[7], Terence G. Langdon[8]

[1] Physics and Chemistry of Materials Lab, Faculty of Sciences, University of M'sila, University Pole, Road Bourdj Bou Arreiridj, M'sila 28000, Algeria
[2] Department of Chemistry, Faculty of Sciences, University of M'sila, University Pole, Road Bourdj Bou Arreiridj, M'sila 28000 Algeria
[3] Laboratory of Materials and Renewable Energy, Faculty of Sciences, University of M'sila, University Pole, Road Bourdj Bou Arreiridj, M'sila 28000, Algeria
[4] Warsaw University of Technology, Faculty of Materials Science and Engineering, Woloska 141, 02-507, Poland
[5] Department of Design and Engineering, Faculty of Science and Technology, Bournemouth University, Poole, Dorset BH12 5BB, UK
[6] Université Paris-Saclay, CNRS, Institut de chimie moléculaire et des matériaux d'Orsay, 91405 Orsay, France
[7] School of Mechanical, Industrial and Manufacturing Engineering, Oregon State University, Corvallis, OR 97331, USA
[8] Departments of Aerospace & Mechanical Engineering and Materials Science, University of Southern California, Los Angeles, CA 90089-1453, USA
* Corresponding author: Pr. Hiba Azzeddine, hiba.azzeddine@univ-msila.dz

Abstract

Bulk pure Cu and Cu-5Fe (wt%) materials were successfully fabricated at room temperature by powder consolidation using high-pressure torsion (HPT) processing through 30 turns under a pressure of 6 GPa. The microstructure, texture and mechanical properties of the fabricated bulk discs were systematically characterized across their diameters using electron backscatter diffraction, scanning electron microscopy, transmission electron microscopy, X-ray diffraction and Vickers microhardness. Additionally, their thermal stability was evaluated after annealing treatment at 500 °C for 6 h. The results show that two grain refinement stages occurred in the Cu disc accompanied by the formation of partial A-fiber (A_1^*/A_2^* and A components). The dynamic recrystallization was delayed in the Cu-5Fe disc owing to the pinning effect of Fe content. Consequently, the grain refinement was more effective and the texture gradually developed the B, A and A_1^* components. The Cu-5Fe disc was harder than the Cu disc and the microhardness increased across the disc diameter. Rapid grain growth with a high amount of Cu_2O oxide and retained texture were the main characteristics of the annealed Cu disc. The precipitation of Fe phase during annealing led to the development of a duplex microstructure at the centre and mid-radius positions and a stable microstructure at the edge of the Cu-5Fe disc. Eventually, the annealing texture was transformed into a complete A-fiber (A_1^*/A_2^* and $A/\bar{A}$ components) which was quite similar to the Cu disc. The microhardness decreased after annealing but it was more homogeneously distributed across the disc diameter than the HPT-processed disc. The results were discussed based on the different grain refinement mechanisms, static recrystallization mechanisms, solute elements, dislocations and annealing twins.

Keywords: Cu-Fe alloy; High-pressure torsion; Powder consolidation; Microstructure; Texture; Thermal stability.

1. Introduction

The association of high thermal conductivity and electrical conductivity of copper (Cu) with the soft magnetic properties and high strength of iron (Fe) by forming Cu-Fe alloys is of great potential interest in applications in high-precision technology fields [1]. However, according to the phase diagram, the Fe-Cu system is fully immiscible in the solid state, making the preparation of Cu-Fe alloys through traditional casting often challenging, especially with high Fe content (>5 wt.%). In fact, the segregation of the Fe phase and the high Fe content in the solid solution can cause a serious microstructural inhomogeneity and decrease the electrical conductivity and the strength of the alloy, thereby restricting the broader application of Cu-Fe alloys [2-4].

Considerable efforts have been made over the past years to develop new material manufacturing routes, including rapid solidification [5], mechanical alloying [6] and a strong magnetic field [7] methods to control the Fe solubility in the Cu matrix, morphology and volume fraction of the Fe phase. Concurrently, other research has focussed on the impact of additional alloying elements in order to produce a uniform microstructure and obtain simultaneous high mechanical and electrical performances of Cu-Fe alloys [8-11]. For example, it was found that the addition of Si and Mg solutes have the ability to reduce the segregation and refine the Fe phase, which is a remarkable advantage for boosting the strength and electrical conductivity of the Cu-Fe alloys [8, 9].

Thermomechanical processing is an effective procedure for tailoring the grain size of the Cu matrix and the size, morphology and distribution of the Fe phase in Cu-Fe alloys [12-18]. However, the results indicate that the microstructures are highly sensitive regarding the deformation and ageing conditions such as strain level and temperature [13, 14, 19]. At present, severe plastic deformation (SPD) processing is an emerging tool for the production of bulk ultrafine-grained materials with enhanced mechanical and functional properties which result from the creation of high densities of lattice defects such as dislocations, vacancies and grain boundaries by using high plastic strains [20]. Among SPD techniques, high-pressure torsion (HPT) processing can introduce outstanding grain refinement (at the nanometer scale) as well as promote phase transformations, such as decomposition or dissolution of phases and even amorphization [21, 22]. In addition, the fabrication of bulk materials by powder consolidation and mechanical bonding chips is easily achieved by HPT processing at room temperature owing to the simultaneous application of a high hydrostatic pressure and torsional shear strain [23-26]. Therefore, many works report the successful feasibility of HPT processing for fabricating Cu-

Fe alloys [27-33]. Nevertheless, the deformation behaviour and the evaluation of the relationship between microstructure, crystallographic texture and mechanical properties of HPT-processed Cu-Fe alloys remain limited [31, 33].

In the current work, bulk Cu-xFe (x = 0 and 5 wt%) alloys were successfully fabricated at room temperature (RT) by powder consolidation using HPT processing through 30 turns under a pressure of 6 GPa. The evolution of microstructure, texture and microhardness across the disc diameters was characterized using different experimental techniques, including electron backscatter diffraction (EBSD), scanning electron microscopy (SEM), transmission electron microscopy (TEM), X-ray diffraction (XRD) and Vickers microhardness. Further, the static recrystallization behaviour of the HPT-processed discs was evaluated after annealing at 500 °C for 6 h.

2. Materials and experimental procedures

The starting materials used in the present study were commercial copper (99.9% purity) and iron (99.9% purity) powders with average particle sizes of 25 and 36 μm, respectively. The powder mixtures with an elemental composition of 5 wt.% Fe and 95wt.% Cu were thoroughly prepared by hand mixing using a mortar and pestle under ambient conditions for 60 min and dispersed by ultrasound treatment for 15 min using a probe sonicator operated at a frequency of 40 kHz to break up any loose agglomerates and increase the uniformity of the mixture. The mixture was pre-compacted at RT using a hand-press machine into a disc shape with a 10 mm diameter and 1 mm thickness with an applied pressure of 450 MPa. Then the discs were consolidated at RT using the HPT processing for 30 turns under a rotation rate of 1 rpm and a pressure of 6 GPa. Based on the existing literature [28, 31, 32], it is believed that such large torsional turns (30 turns) and high applied pressure (6 GPa) would be sufficient to produce a consolidated Cu-Fe material with homogeneous nanostructure.

The HPT processing was conducted under quasi-constrained conditions [34] to restrict the outward flow of material around the periphery of the disc during the processing operation. Precautions were taken throughout the HPT processing to avoid slippage between the disc sample and anvils [35]. Furthermore, the temperature rise during HPT processing is relatively low, which will not have a subsequent effect on the development of microstructure and texture [36].

The deformed discs were then subjected to annealing treatment at 500 °C for 6 h in a radiation furnace, followed by air quenching. The selection of the heat treatment condition was based on

prior studies, which indicated that the optimal aging temperature of Cu-Fe alloys is typically around 500 °C [1].

The discs were cut into two halves along their mid-plane. As illustrated in Figure 1, the microstructural observations, texture and microhardness measurements were performed on the cross-sectional (CD-SD) planes of the HPT-processed and annealed discs. For information, the shear reference frame is defined as the shear direction (SD), radial direction (RD) and compression direction (CD).

It should be noted that when the number of HPT turns was above 5 turns, there was no recovery or self-annealing at RT during the storage time of the HPT-processed pure Cu [37].

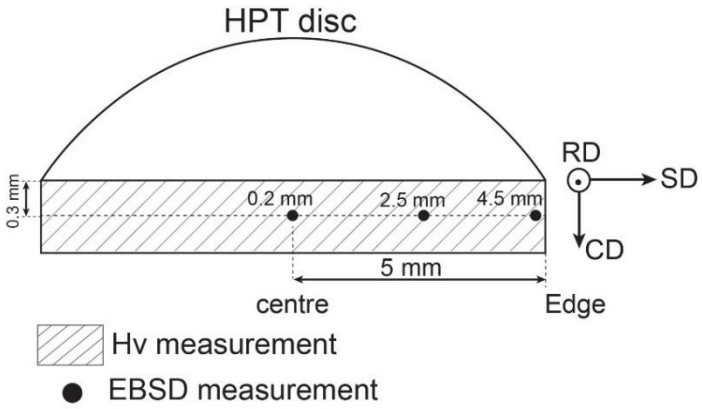

Figure 1: Schematic illustration indicating the positions for the EBSD and microhardness measurements on the vertical cross-section of the HPT disc. SD, CD, and RD are the coordinate systems.

The EBSD measurements were performed near the centre (r ~ 0.2 mm), at the mid-radius position (r ~ 2.5 mm) and the edge (r ~ 4.5 mm) of the mid-thickness plane of the HPT-processed and annealed discs (see Figure 1) using a TSL-EDAX-Hikari system mounted on a scanning electron microscope (FEG-SEM ZEISS Supra 55 VP) operating at 20 kV. Sample preparation for the EBSD measurements consisted of mechanical polishing using SiC abrasive papers up to 4000-grid, followed by diamond polishing up to 0.25 µm and then a final polishing using oxide polishing suspensions (OPS).

Data collected from scanned areas of 25 × 25 μm^2 with a 25 nm step size were treated by the Orientation Imaging Microscopy OIM^{TM} software. The scanned areas for the annealed Cu discs were 50 × 50 μm^2 with a step size of 50 nm. A grain tolerance angle of 5°, a minimum grain size of 5 pixels and a confidence index (CI) < 0.05 were chosen as a clean-up procedure for the quantitative EBSD analyses. The grain boundaries were classified into sub-grain boundaries

with misorientations 2°< θ < 5°, low-angle grain boundaries (LAGBs) with misorientations 5°< θ < 15° and high-angle grain boundaries (HAGBs) with θ > 15°. Grain boundaries with misorientation angles θ < 2° were removed to avoid spurious boundaries caused by orientation noise.

The dynamically recrystallized fraction in the HPT-processed discs was estimated using the grain orientation spread (GOS) approach implemented in the OIM™ software, where the GOS is known as the mean deviation between the orientation of each point in the grain and the mean orientation of the grain [38]. In the present case, grains with GOS < 1° are assumed to be completely recrystallized [38].

The kernel average misorientation (KAM) approach was used to estimate the stored energy, E_s, originating from the geometrically necessary dislocation (GNDs), following the equation [39]:

$$E_s = \frac{\alpha \mu b \theta_{KAM}}{2nd} \quad (1)$$

where α is a parameter that depends on the grain boundary type with values of 2 and 4 for pure tilt and twist boundaries, respectively [40], μ = 48.3 GPa is the shear modulus for Cu [39], b = 0.255 nm is the magnitude of the Burgers vector for Cu [39], θ_{KAM} is the average misorientation angle, n = 3 for the nearest neighbor and d = 25 nm is the EBSD scan step size. In the present case, the θ_{KAM} value was calculated from the average misorientation angle between the point and its 3rd neighbor (n = 3) excluding misorientations greater than 5°.

The texture was quantified using toolbox MTEX by calculating the orientation distribution function (ODF) using the harmonic method (L = 22) and a Gaussian function with a half-width of 5° to model each orientation [41].

A scanning electron microscope (SEM), Hitachi SU8000, operating at an accelerating voltage of 10 kV in backscattered electron (BSE) mode and equipped with an energy-dispersive spectrometer (EDS), was used to identify the chemical elements of various phases present near the mid-radius position of the HPT-processed Cu-5Fe disc. Specimens for SEM were prepared via grinding and ion polishing on Hitachi Ion Milling System IM-4000. The ion milling is a damage-less process, so that the polishing with the ion beam eliminates all deformation, stresses and oxide layers. Moreover, the surface quality is sufficiently good that the structure of such prepared joints can be observed on an SEM microscope through the channeling contrast.

Detailed structural investigations were further carried out using a Thermo Fisher Scientific SPECTRA 200 scanning transmission electron microscope (STEM), featuring a dedicated Cs-corrected high-resolution system operating at an accelerating voltage of 200 kV and achieving a spatial resolution of 75 pm. Chemical analyses were performed using a next-generation Super-

X EDX system, equipped with four state-of-the-art detectors, each offering an increased collection solid angle of 0.7 sr. STEM samples were extracted from the mid-radius region of the discs using a galium focused ion beam (FIB) microscope (Hitachi NB-5000), following a standard cutting procedure [42].

The X-ray diffraction (XRD) patterns were recorded on the RD-SD plane of the discs using an X'PERT PRO MPD diffractometer operating at 40 kV and 40 mA with Cu-K radiation (λ = 0.1541 nm). The data were collected over a range of 2θ = 10–80° with a step size of 0.02°.

Vickers microhardness measurements were taken using a Mitutoyo HM-200 with a load of 50 gf and a dwell time of 10 s. The discs were cut vertically across the diameters and the cross sections were polished to mirror-like surfaces. A series of hardness values were recorded on these cross-sections, measuring 8000 × 450 μm^2, where a rectilinear grid pattern (see Figure 1), having 150 µm separation between adjacent points, was applied for the automated measurement procedure. The recorded hardness values gave a total of 248 points, and these points were used for the construction of color-coded contour maps.

3. Results

3.1. XRD and SEM characterization

Figure 2 presents the XRD patterns of the HPT-processed and annealed Cu and Cu-5Fe discs. Both HPT-processed Cu (Figure 2a) and Cu-5Fe (Figure 2b) discs exhibit peaks belonging only to the Cu matrix. This indicates the possible formation of a solid solution state in the HPT-processed Cu-5Fe disc. For confirmation, Figure 3 displays the SEM images with different magnifications and EDS analysis taken near the mid-radius position of the HPT-processed Cu-5Fe disc. For comparison, an SEM photo showing the microstructure near the mid-radius of the HPT-processed Cu disc is displayed in Figure 3c. It can be observed that the formation of the granular microstructure is decorated by numerous black zones of different sizes.

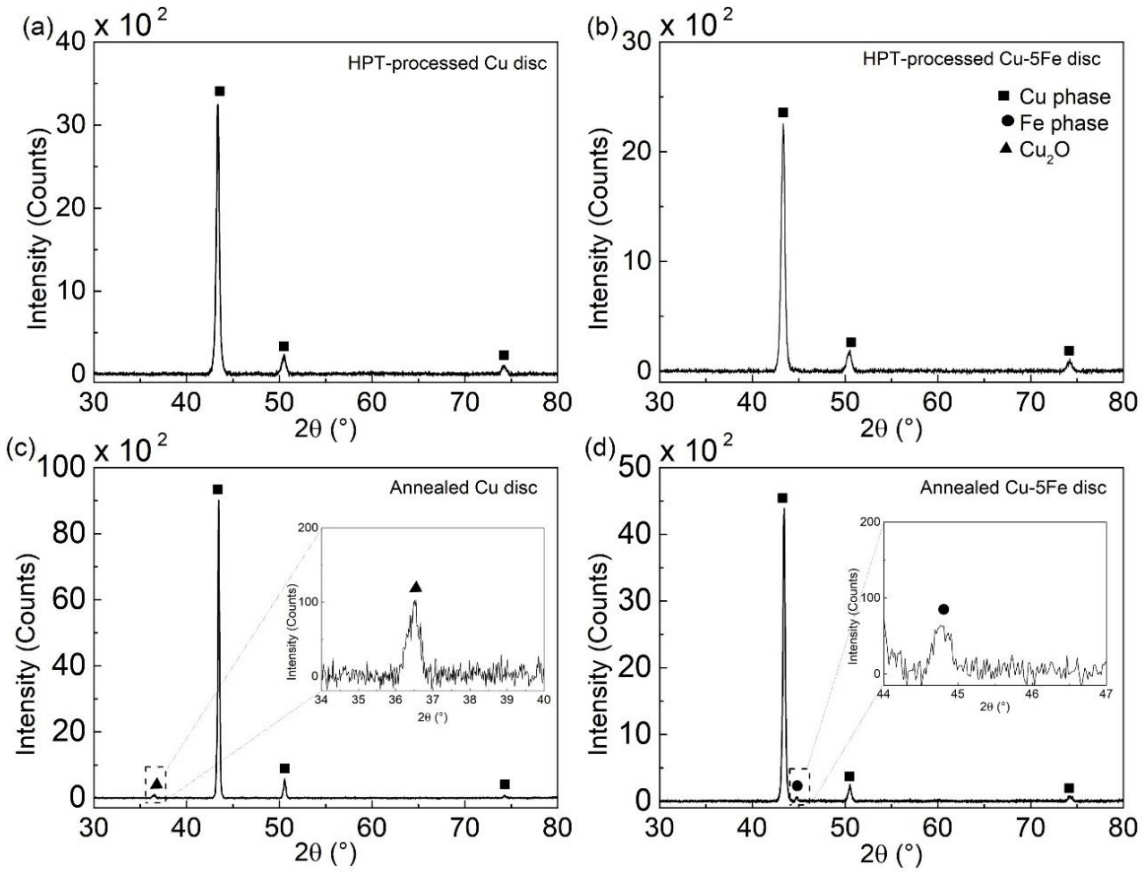

Figure 2: XRD patterns of (a) HPT-processed Cu disc, (b) HPT-processed Cu-5Fe disc, (c) annealed Cu disc and (d) annealed Cu-5Fe disc.

The EDS analysis of point 1 demonstrates the formation of a solid solution containing almost 5% of Fe element (Fig. 3b). The presence of high content of Fe (74.4±0.7%) and O (22.5±0.2%) elements in the black zone (Point 2) indicated the formation of the iron oxide (Fe_2O_3) phase.

The absence of peaks belonging to the Fe_2O_3 phase in the XRD pattern of the HPT-processed Cu-5Fe disc may indicated the low fraction of this phase. As shown in Figure 3c, a granular microstructure is also reached for the HPT-processed Cu disc. The microstructure is decorated by black spots homogenously distributed, as indicated by the arrows. It was not possible to identify these black spots due to their small size but it may be copper oxide (Cu_2O).

Figure 2c shows that annealing at 500 °C for 6 h causes the formation of Cu_2O oxide in the annealed Cu disc, as indicated by the development of a peak around $2\theta = 36.5°$. In the case of the annealed Cu-5Fe disc, the XRD pattern in Figure 2d demonstrates the development of a small peak around $2\theta = 44.7°$ belonging to the Fe phase, thereby confirming a precipitation of the α-Fe phase during the annealing treatment.

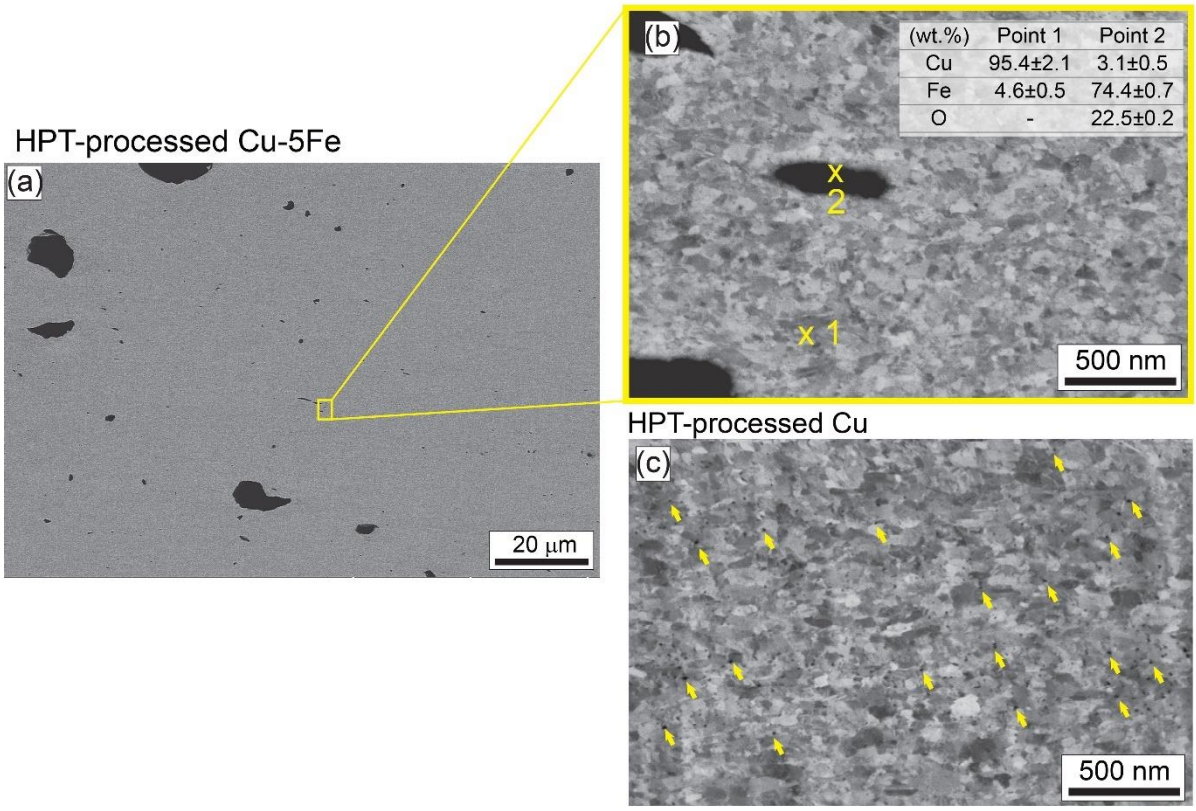

Figure 3: SEM photos with (a) low and (b) high magnification showing the microstructure near the mid-radius of the HPT-processed Cu-5Fe disc, EDS analysis at points 1 and 2 present in Figure 3b and (c) SEM photo showing the microstructure near the mid-radius of the HPT-processed Cu disc. The arrows in Figure 3c indicate the presence of small black spots.

3.2. EBSD characterization across the disc diameter

The EBSD results revealed the presence of Fe grains in the HPT-processed and annealed Cu-5Fe discs. Thus, for the sake of clary the microstructural characterizations of the Cu and Fe grains across the disc diameters were separated into 2 sections.

3.2.1. Microstructure evolution of Cu grains across the disc diameter

The microstructure in the centre, mid-radius and edge on mid-thickness planes of the HPT-processed and annealed Cu and Cu-5Fe discs represented in the form of inverse pole figure (RD-IPF) maps are shown in Figures 4 and 5, respectively. In the RD-IPF maps, the HAGBs are indicated by black lines. Enlarged zones were inserted in the upper right corner of some RD-IPF maps to easily visualize the Cu grain structure of the samples.

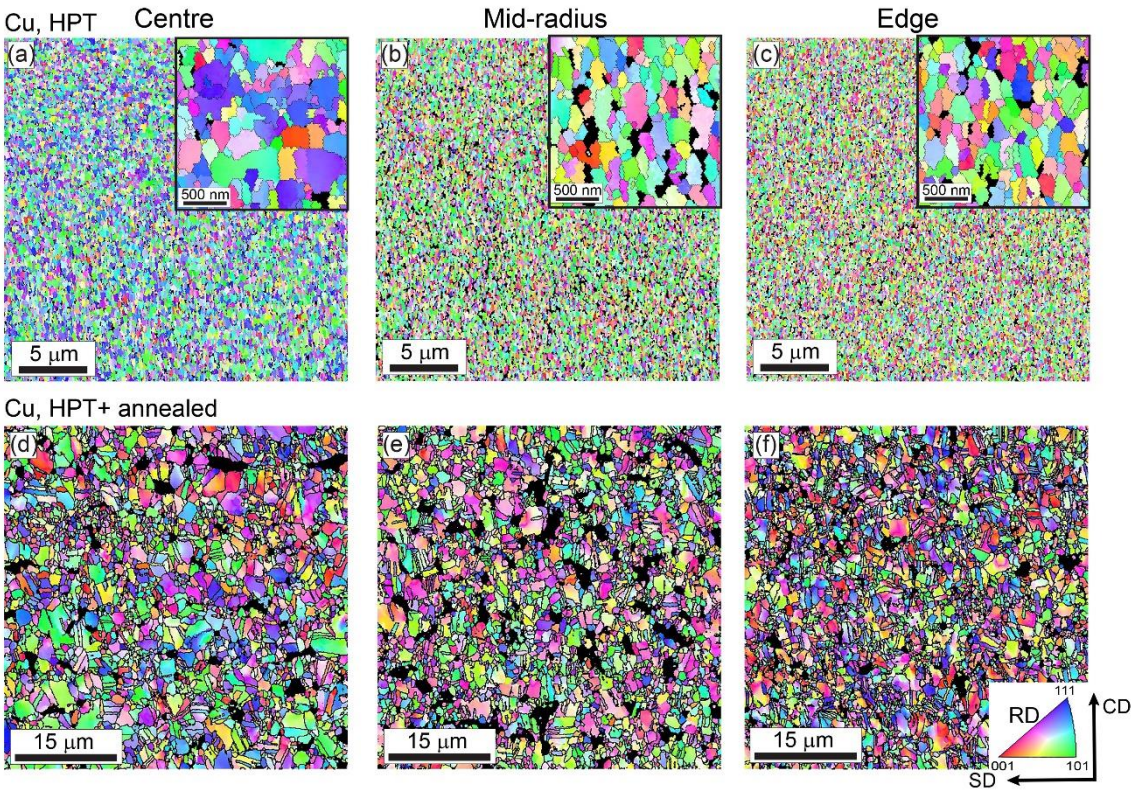

Figure 4: RD-IPF maps at: (a, d) the centre, (b, e) mid-radius and (c, f) edge of HPT-processed and annealed Cu discs, respectively. The color-coded triangle is shown in the bottom right corner of the RD-IPF map (Figure 4f). The grains in the IPF maps are coloured based on their crystallographic directions with respect to RD. Enlarged zones were inserted to visualize the Cu grain structure of the HPT-processed Cu disc (in Figures 4a-c).

Thus, Figure 6 displays the evolution of the mean grain size of the Cu grains and HAGBs fraction as a function of the distance from the centre of the HPT-processed and annealed Cu and Cu-5Fe discs, respectively.

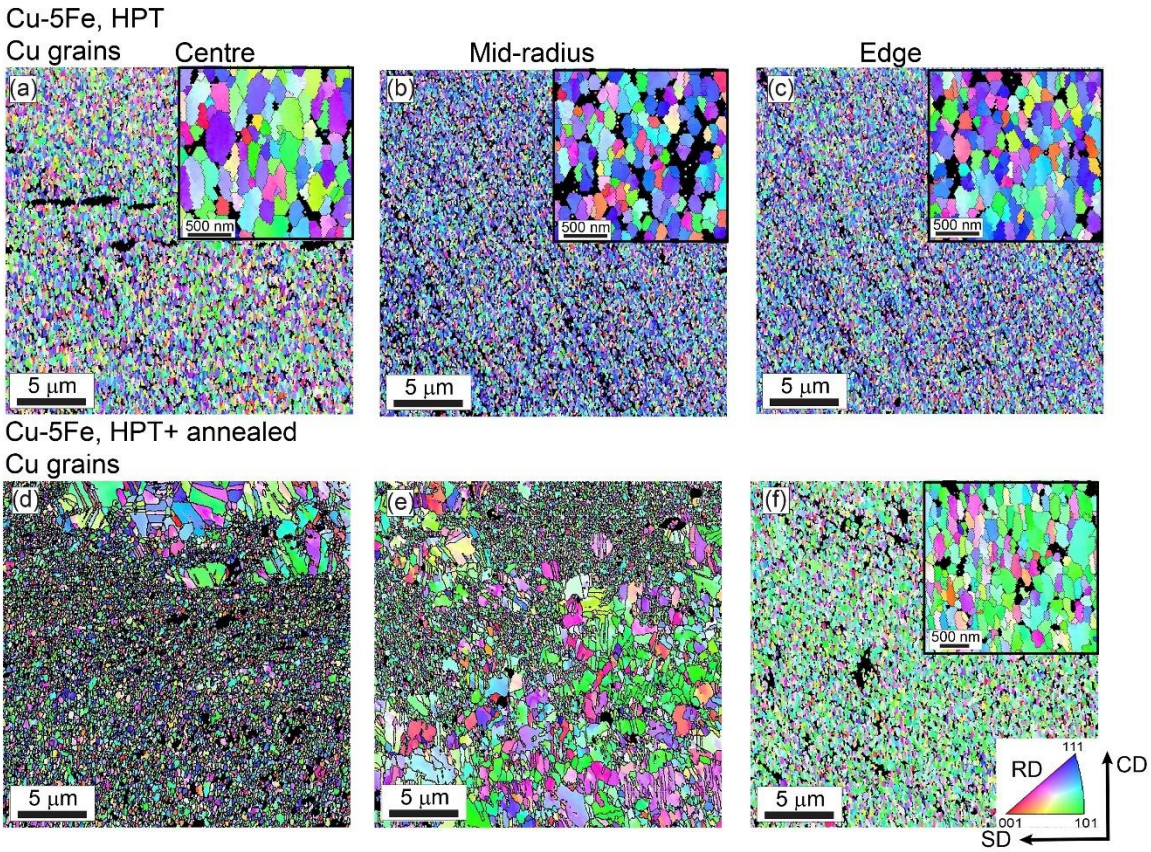

Figure 5: RD-IPF maps showing the Cu grains at: (a, d) the centre, (b, e) mid-radius and (c, f) edge of HPT-processed and annealed Cu-5Fe discs, respectively. The color-coded triangle is shown in the bottom right corner of the RD-IPF map (Figure 5f). The grains in the IPF maps are coloured based on their crystallographic directions with respect to RD. Enlarged zones were inserted to visualize the Cu grain structure of the HPT-processed (in Figures 5a-c) and annealed Cu-5Fe (in Figure 5f) discs.

In the case of the HPT-processed Cu disc, the zoomed area at the centre position (Figure 4a) shows the formation of equiaxed grains with a mean grain size of around 272 ±30 nm. The grains became elongated along SD (see Figures 4b and 4c) and the mean grain size decreased to 224 ± 20 and 200 ± 15 nm (Figure 6a) at the mid-radius and edge positions, respectively. A net change in grain orientation across the diameter is noticeable. The evolution of texture will be presented in detail later. A microstructure consisting of 76% of HAGBs is obtained at the centre but this is decreased to 62% at the mid-radius and then increased again to 78% at the edge of the HPT-processed Cu disc (Figure 6b).

Table 1 presents the evolution of dynamic recrystallization (DRX) fraction and the stored energy as a function of distance from the centre of the HPT-processed Cu and Cu-5Fe discs, respectively. It is worth noting that the stored energy has been estimated from GND dislocations

and in practice additional stored energies from other lattice defects, such as statistically stored dislocations and vacancies, may be also present in the severely deformed microstructure and contribute to dynamic and static recrystallization [43, 44].

As can be seen, already half of the microstructure at the centre of the HPT-processed Cu disc is dynamically recrystallized (50.8%). The stored energy at the centre was found to be equal to 35.1 J/mol, but the fraction of DRX decreased (39.1%) and the stored energy increased (43.5 J/mol) at the mid-radius position. At the edge of the HPT-processed Cu disc, the fraction of DRX increases again (64.1%), which causes a decrease in the stored energy to 34.4 J/mol.

In the case of the HPT-processed Cu-5Fe disc, the RD-IPF map of the enlarged area (Figure 5a) at the centre position shows the development of elongated grains along the SD with a mean Cu grain size equal to 250 ±25 nm. The grain structure became smaller and equiaxed at the mid-radius (Figure 5b) and the edge (Figure 5c) positions and the mean grain size saturated at a value of 190 ±20 nm (Figure 6c). A microstructure consisting of 60% of HAGBs is obtained at the centre and the fraction of HAGBs increases slightly to 67% at the edge of the HPT-processed disc (Figure 6d). It can be observed that the modification in the orientation of grains across the diameter is not drastic by comparison with the HPT-processed Cu disc. Table 1 shows that the fraction of DRX increases gradually from 26.4% at the centre to 31.8 and 33.4 % at the mid-radius and edge positions, respectively, whereas the stored energy is found to be similar (~44.7 J/mol) at these three positions.

Table 1. Fraction of DRX and stored energy at the centre, mid-radius and edge of the HPT-processed Cu and Cu-5Fe discs.

	HPT-processed Cu		HPT-processed Cu-5Fe	
	DRX (%)	E_s (J/mol)	DRX (%)	E_s (J/mol)
Centre	50.8	35.1	26.4	44.4
Mid-radius	39.1	43.5	31.8	44.7
Edge	64.1	34.4	33.4	44.7

Figures 4d-4f show that a typical recrystallization microstructure of annealed bulk Cu-based alloys is developed in the HPT consolidated Cu disc after the annealing treatment. However, there are many black zones (not indexed areas) which, according to the XRD results (Figure 2c), could originate from the Cu_2O oxide particles. The coarse grains are decorated with numerous annealing Σ3 (60°<111>) twin boundaries and the estimated fraction of annealing twins was 20, 21 and 15% at the centre, mid-radius and edge of the annealed Cu discs, respectively. According to Figure 6a, the nanostructure of the HPT-processed Cu disc was lost

after annealing in which the mean grain size increased significantly to 2.2 ± 1.1, 1.9 ± 1.3 and 1.6 ± 1.5 μm at the centre, mid-radius and edge positions, respectively. For additional information, note that the mean grain size was measured by excluding the twin boundaries. In contrast, the HAGBs fraction decreases after the annealing treatment to ~56% at the three positions by comparison with the HPT-processed Cu disc (see Figure 6b).

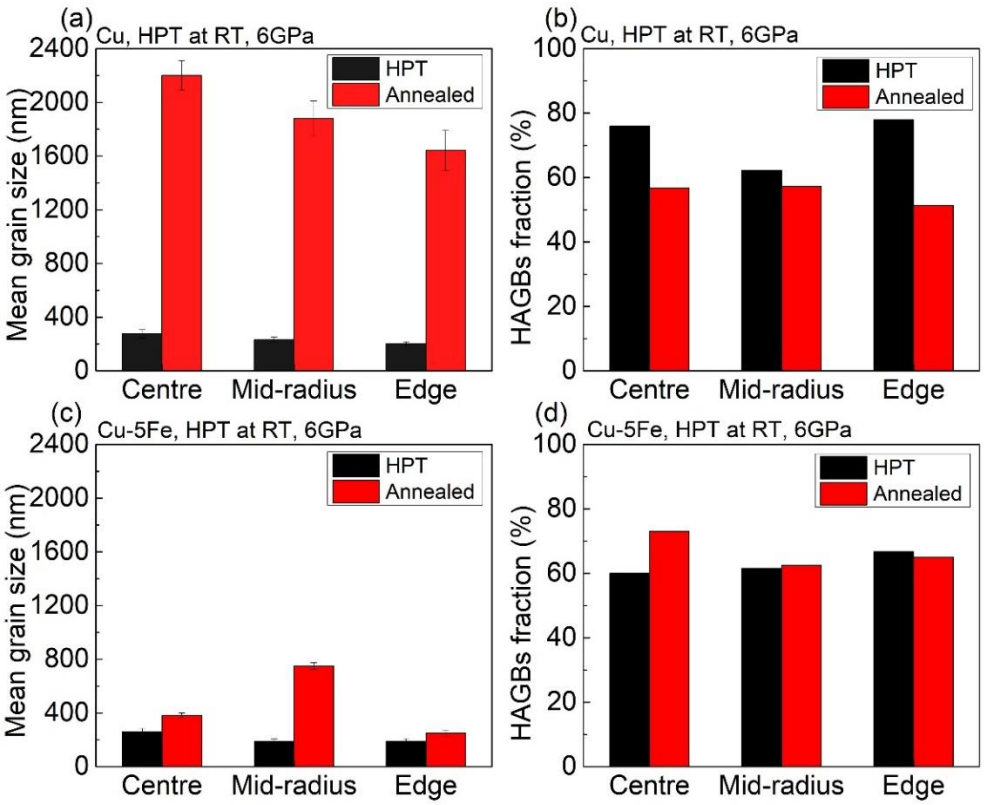

Figure 6: Evolution of mean grain size and HAGBs fraction at the centre, mid-radius and edge of the HPT-processed and annealed: (a, b) Cu and (c, d) Cu-5Fe discs, respectively.

The microstructure of the annealed Cu-5Fe disc across the diameter is quite different from the annealed Cu disc. Annealing at 500 °C for 6 h of the HPT-processed Cu-5Fe disc leads to the formation of a duplex microstructure formed principally of coarse grains and nano-sized grains at the centre and mid-radius positions of the disc (see Figures 5d and 5e). The heterogeneous microstructure is more pronounced at the mid-radius position. Similar to the annealed Cu disc, the larger grains contain several annealing twins and the fraction of twins at the centre and mid-radius was found to be around 6 and 14%, respectively. Consequently, the mean Cu grain size at the centre and mid-radius increases to 380 ±2 0 and 750 ± 25 nm, respectively. In contrast, the microstructure at the edge position of the annealed Cu-5Fe disc remains homogenously

equiaxed nano-sized grains (Figure 5f) but the mean grain size increases to 250 ± 20 nm (Figure 6c). The fraction of HAGBs shown in Figure 6d does not change significantly from the HPT-processed Cu-5Fe disc, except for a slight increase at the centre of the annealed disc (75%). These results originate from the capacity of HPT processing for producing refined microstructures with relatively higher fractions of HAGBs [45].

3.2.2. Microstructure evolution of Fe grains across the disc diameter

Figure 7 presents the RD-IPF maps showing the Fe grains at the centre, mid-radius and edge of the HPT-processed and annealed Cu-5Fe discs, respectively.

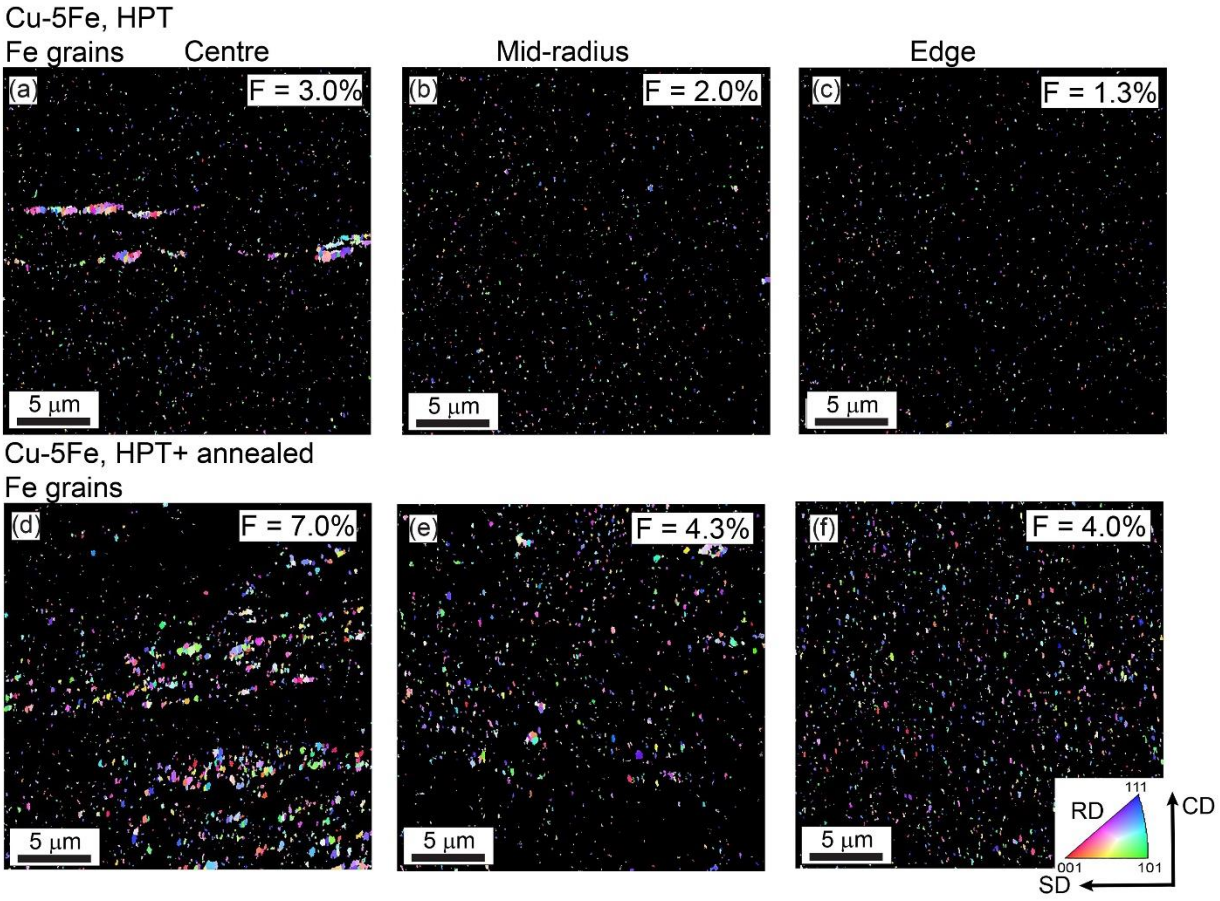

Figure 7: RD-IPF maps showing the Fe grains at: (a, d) the centre, (b, e) mid-radius and (c, f) edge of HPT-processed and annealed Cu-5Fe discs, respectively. The color-coded triangle is shown in the bottom right corner of the RD-IPF map (Figure 7f). The grains in the IPF maps are coloured based on their crystallographic directions with respect to RD. The fraction of Fe grains is indicated in the upper right corner of the RD-IPF maps.

The fraction of Fe grains in each position, estimated based on the OIM software, is displayed in the upper right corner of each RD-IPF maps. In contrast to the XRD results (Figure 2b), the EBSD measurements revealed the presence of the Fe phase, as in Fe grains, in the HPT-processed Cu-5Fe disc. According to the OIM software, the Fe phase fraction estimated at the centre was relatively weak, about 3% and it seems to decrease to 1.7% and 1.3% at the mid-radius and the edge of the disc, respectively. This could explain why the Fe phase was not detected by XRD analysis. Furthermore, the shape and the distribution of the Fe phase are also affected by the measured position. It can be observed that the Fe phase at the centre of the disc (Figure 7a) is in the form of a band parallel to SD and then becomes smaller and uniformly distributed towards the edge of the HPT-processed Cu-5Fe disc (Figures 7b and c).

The mean grain sizes of the Fe grains in the HPT-processed and annealed Cu-5Fe discs are summarized in Table 2. It is worth noting that further microstructural features for the Fe grains, such as the HAGBs fraction, were not evaluated because of their low values and their arbitrary distribution in the EBSD maps.

Table 2. Evolution of mean grain size of Fe grains as a function of distance from the centre of HPT-processed and annealed Cu-5Fe discs.

Grain size of Fe grains (nm)	Centre	Mid-radius	Edge
HPT-processed Cu-5Fe	250±15	139±10	125±10
Annealed Cu-5Fe	270±20	220±15	170±20

Table 2 indicates that the Fe grains at the centre position exhibits a value of 250 ± 15 nm and it decreases continuously with increasing the distance from the centre of the disc to reach a value of 125 ± 10 nm at the edge position.

Figures 7d-7f revealed that the fraction of the Fe phase increases with respect to the deformation state to 7.0, 4.3 and 4.0% at the centre, mid-radius and edge of the annealed Cu-5Fe disc, respectively, and their size becomes larger after annealing as is evident by Table 2. The mean grain size of the Fe grains increases to 270 ± 20, 220 ± 15 and 170 ± 20 nm at the centre, mid-radius and edge of the annealed Cu-5Fe disc, respectively.

3.3.STEM characterization

Figure 8 presents additional microstructural observations taken near the mid-radius of the HPT-processed Cu and Cu-5Fe discs using STEM in BF and HAADF modes with different magnifications. The STEM photos in BF of the HPT-processed Cu (Figure 8a) and Cu-5Fe

(Figure 8d) discs revealed the development of nanocrystalline grain structures which were relatively homogeneously distributed through the microstructures. The STEM images in the HAADF mode provide evidence of nano-sized particles with a circular shape of copper oxide (blue arrows) in the HPT-processed Cu disc (Figure 8b) and iron oxide (red arrows) in the HPT-processed Cu-5Fe disc (Figure 8e). In Figure 8c, a stacking fault (green arrow) and nano-sized lamella deformation twins (yellow arrows) are visible in the HPT-processed Cu disc. The HPT-processed Cu-5Fe disc also revealed the presence of nano-sized twins as indicated by the yellow arrow in Figure 8d.

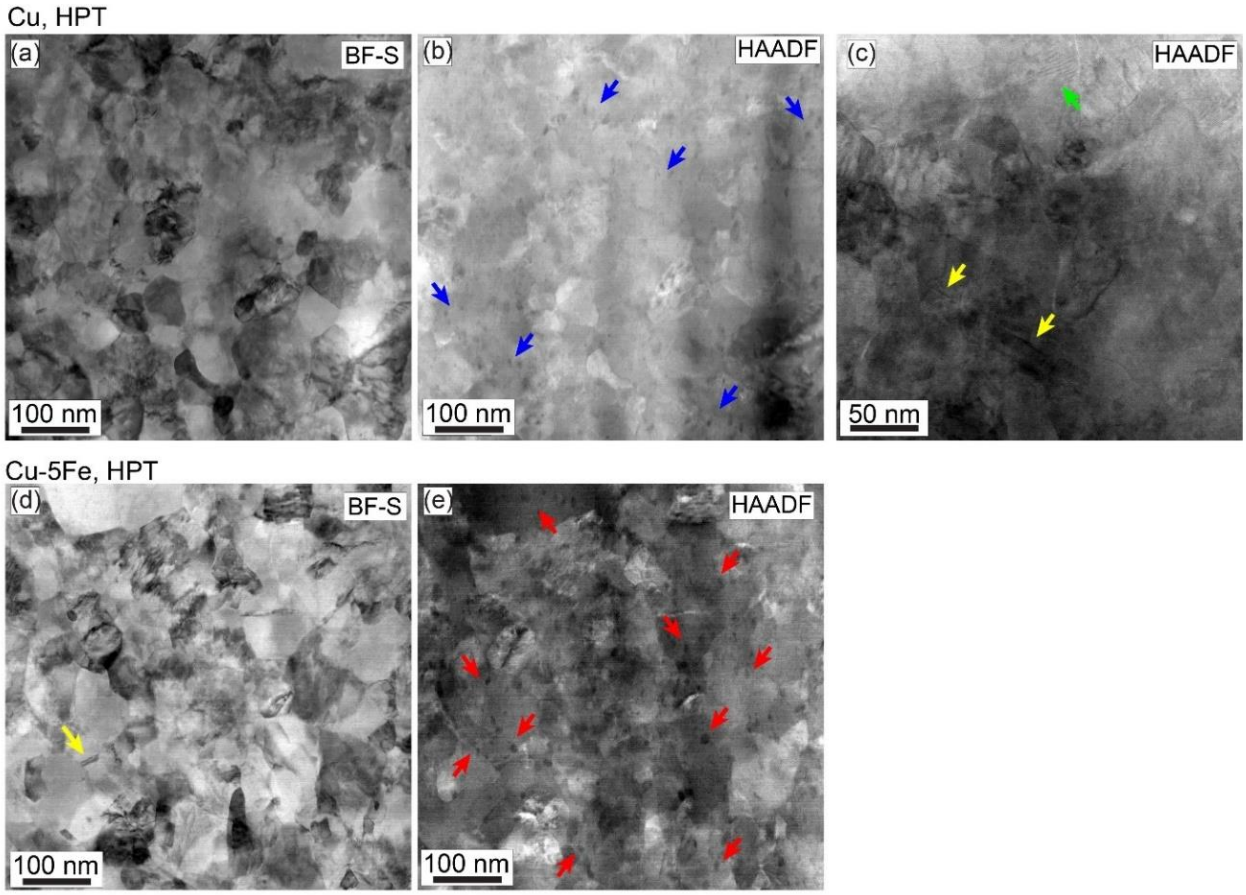

Figure 8: STEM images in BF and HAADF modes for the HPT-processed: (a-c) Cu and (d, e) Cu-5Fe discs, respectively.

Figure 9 depicts the STEM images in BF and HAADF modes with the corresponding EDS mapping for the Cu, Fe and O elements for the annealed Cu-5Fe disc, respectively. Similar to the EBSD results (Figure 5e), the STEM image shows the development of a duplex microstructure after the annealing treatment. Annealing twins are easily recognized, as indicated by the yellow arrow in Figure 9a. Interesting findings can be seen from the STEM

and EDS mapping in which the small refined grains are surrounded by large (~ 160 nm) and nano-sized (~ 70 nm) iron oxide Fe_2O_3 particles while the coarse grains are completely free from Fe and O elements. A close inspection of Figure 9d reveals the homogenous distribution of the Fe element in the region with small grains which means that the nano-sized grains achieve a uniform solid solution state.

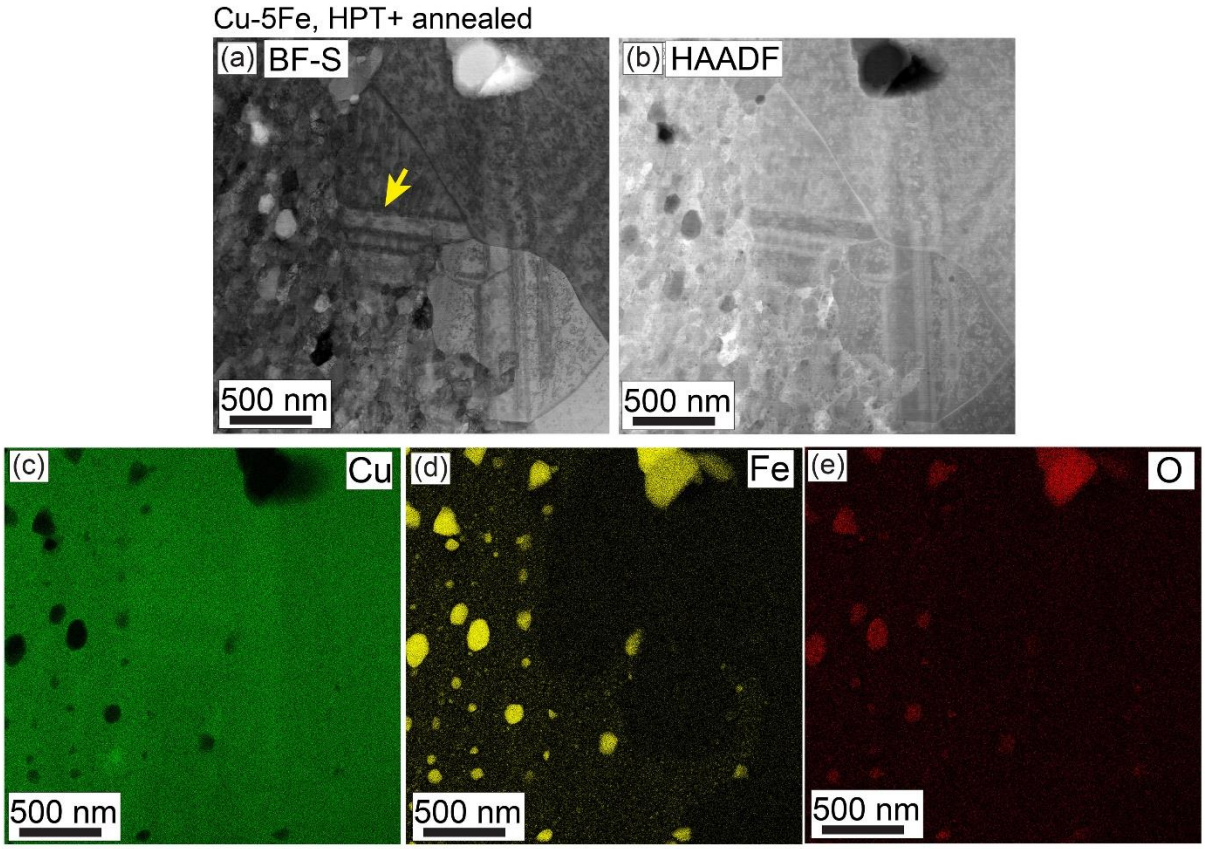

Figure 9: STEM image in (a) BF and (b) HAADF modes with the corresponding EDS mapping for (c) Cu, (d) Fe and (e) O elements for the annealed Cu-5Fe disc, respectively.

3.4.Texture evolution across the disc diameter

3.4.1. Texture evolution of Cu grains across the disc diameter

Figures 10 and 11 present the ODF sections at $\varphi_2 = 0$ and 45° at the centre, mid-radius and edge of the HPT-processed and annealed Cu and Cu-5Fe discs, respectively. It must be noted that the ODF sections presented in Figure 11 show the texture of Cu grains in the HPT-processed and annealed Cu-5Fe discs. The positions of the ideal shear texture components for FCC materials are indicated in the ODF sections and their description in Miller indices ({hkl}<uvw>) and Euler angles (φ_1, Φ, φ_2) are summarized in Table 3 [46]. Basically, HPT processing led to the formation of a simple shear texture type characterized by the formation of two fibers [46]. Thus,

the A-fiber ({111}// RD-SD plane) contained the A, $\bar{A}$, A_1^* and A_2^* components [46] and the second fiber named B-fiber (<110>}// SD) contained the A, $\bar{A}$, B, $\bar{B}$, and C components [46].

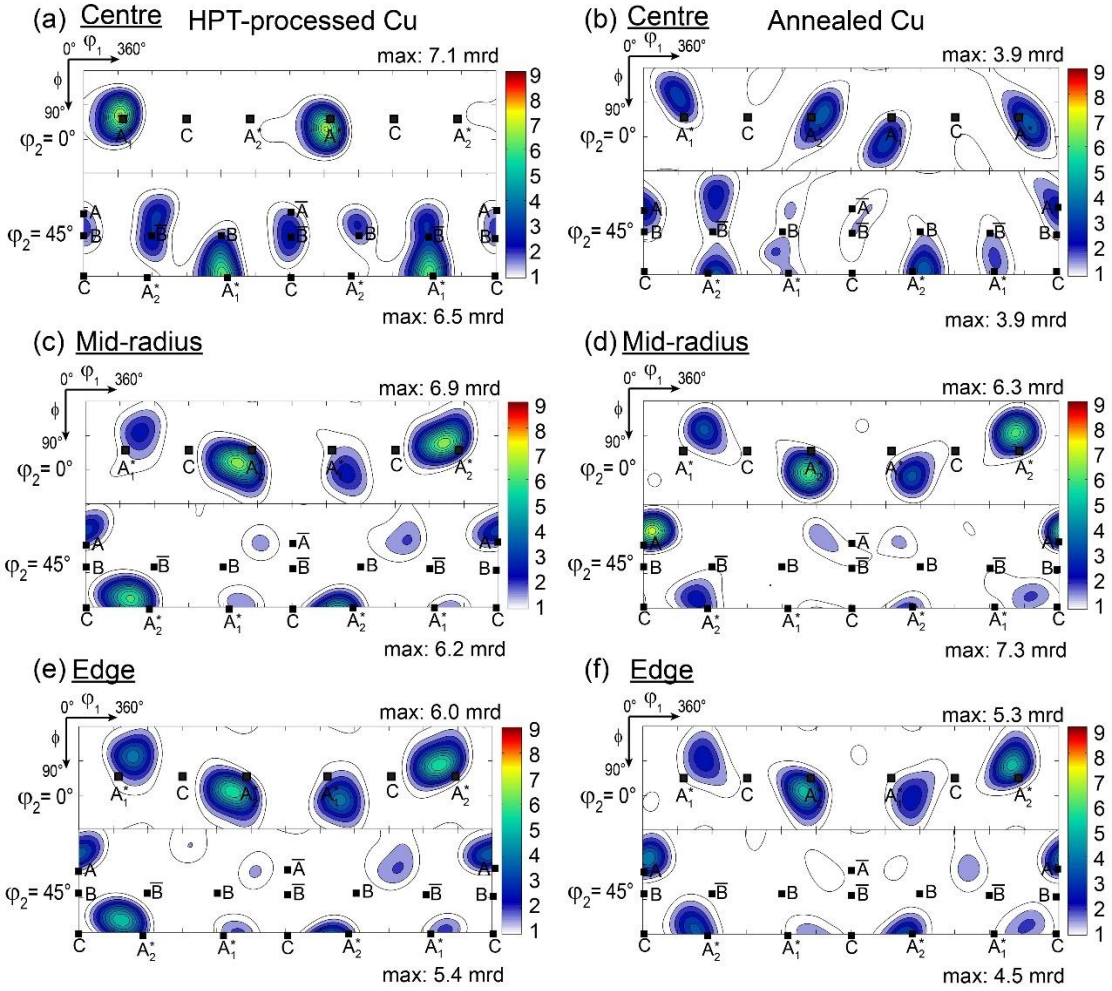

Figure 10: ODF sections at $\varphi_2 = 0$ and 45° at: (a, b) the centre, (c, d) mid-radius and (e, f) edge of HPT-processed and annealed Cu discs, respectively. The positions of the ideal shear texture components are indicated in the ODF sections.

At the centre of the HPT-processed Cu disc (Figure 10a), the texture exhibits the formation of partial B-fiber (presence of $B/\bar{B}$, and $A/\bar{A}$ components and absence of C component) and partial A-fiber (presence of $A/\bar{A}$, A_1^* components and absence of A_2^* component) with a strong A_1^* component (6.5 mrd, multiple random distribution). The texture components belonging to the A-fiber and B-fiber are located in their ideal positions. The texture completely changes at the mid-radius position (see Figure 10c), where B and $\bar{B}$ disappeared and the A and A_2^* components appeared with an obvious deviation from their ideal positions and the spread of the A_2^* orientation. Thus, the partial B-fiber vanished, while the partial A-fiber persists but with the

presence of A and A_1^*/A_2^* components and the absence of the $\bar{A}$ component. Figure 10e shows that the texture at the edge of the HPT-processed Cu disc is very similar to that at the mid-radius position.

Table 3. Ideal position of shear texture components for FCC and BCC materials projected in the SD-CD plane [46].

Shear texture for FCC materials			**Shear texture for BCC materials**		
Notation	Miller indices {hkl}<uvw>	Euler angles (°) (φ_1, Φ, φ_2)	Notation	Miller indices {hkl}<uvw>	Euler angles (°) (φ_1, Φ, φ_2)
A	{112}<1$\bar{1}$0>	(0, 35.2, 45)	D_1	{011}<1$\bar{1}$1>	(54.7, 45, 0)
$\bar{A}$	{211}<0$\bar{1}$1>	(50.7, 65.9, 63.4)	D_2	{011}<$\bar{1}$11>	(125.2, 45, 90)
A_1^*	{101}<$\bar{1}\bar{2}$1>	(35.26, 45, 90)	J	{111}<$\bar{1}\bar{1}$2>	(90, 54.7, 45)
A_2^*	{011}<$\bar{2}\bar{1}$1>	(144.7, 45, 0)	$\bar{J}$	{111}<1$\bar{2}$1>	(30, 54.7, 45)
B	{111}<1$\bar{1}$0>	(0, 57.4, 45)	E	{112}<$\bar{1}\bar{1}$1>	(90, 35.2, 45)
$\bar{B}$	{111}<0$\bar{1}$1>	(60, 54.7, 45)	$\bar{E}$	{112}<11$\bar{1}$>	(270, 35.2, 45)
C	{110}<1$\bar{1}$0>	(0, 90, 45)	F	{011}<100>	(0, 45, 0)

{hkl}//SD-CD plane, <uvw>//CD

Annealing at 500 °C for 6 h maintained the deformation texture reasonably across the distance from the centre of the Cu disc. As can be seen from Figure 10b, the A_2^* component appeared and the intensity of the partial B-fiber decreased at the centre of the annealed Cu disc. The deformation texture was principally retained at the mid-radius position (Figure 10d) but with strengthening of the A component (7.3 mrd). The texture at the edge of the annealed Cu disc (Figure 10f) was retained and tends to be weaker with respect to the texture of the HPT-processed Cu disc.

For the HPT-processed Cu-5Fe disc, the ODF sections at the centre of the disc, shown in Figure 11a, indicated the presence of the A_2^* component with the gradual formation of partial B-fiber due to the presence of the C and B components but with a visible deviation from their ideal positions. Figures 11c and 11e revealed that the textures at the mid-radius and edge positions are identical, where the C component disappeared and a net strengthening of the A_2^* and B components is noted. In both mid-radius and edge positions, a maximum texture intensity of 8.7 mrd is located between the A_2^* and B components at (220°, 65°, 45°), as indicated by the arrow in the ODF section at $\varphi_2 = 45°$ (Figures 11c and 11e).

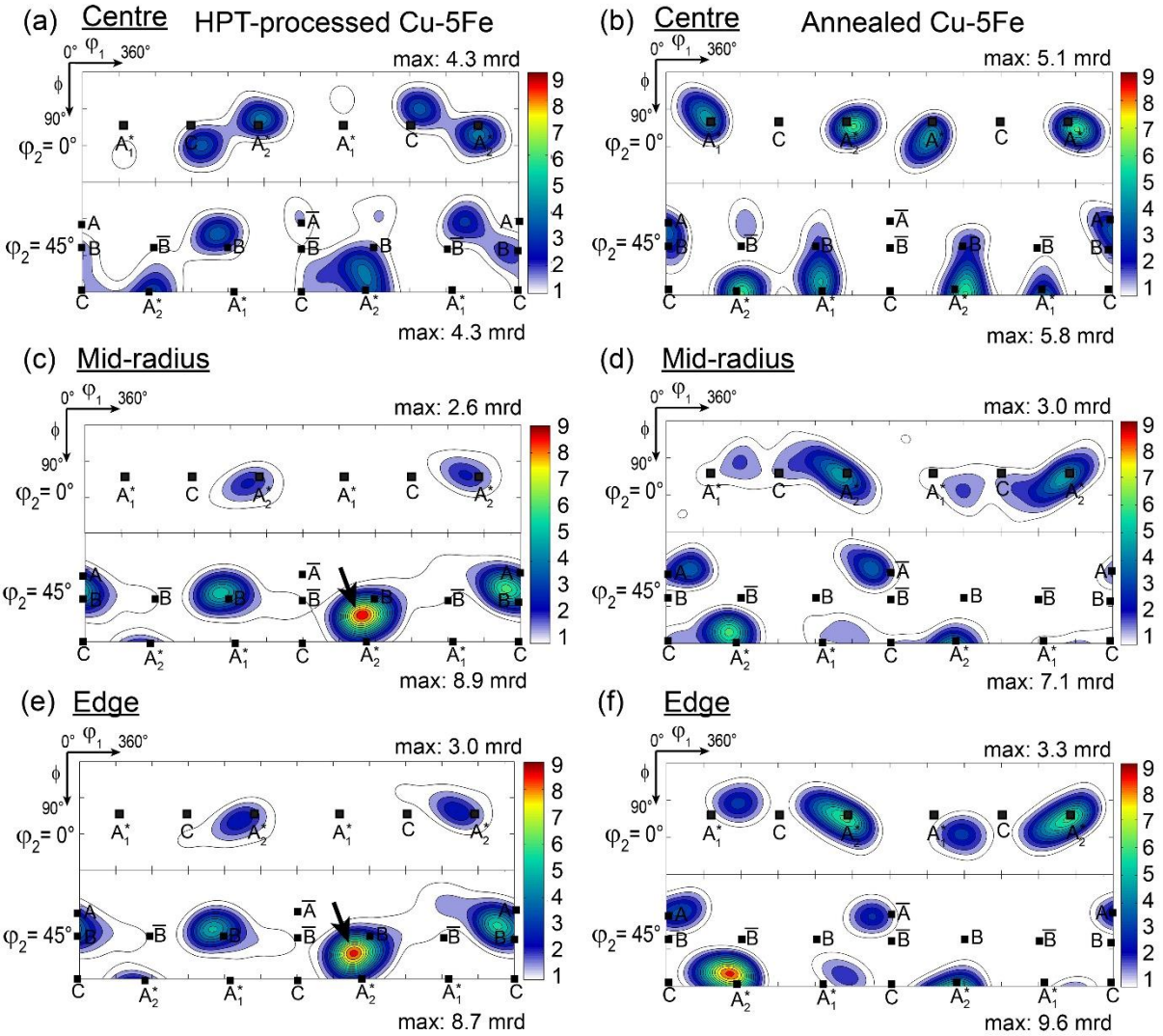

Figure 11: ODF sections at φ_2 = 0 and 45° showing the texture of the Cu grains at: (a, b) the centre, (c, d) mid-radius and (e, f) edge of HPT-processed and annealed Cu-5Fe discs, respectively. The positions of the ideal shear texture components are indicated in the ODF sections.

The texture at the centre of the annealed Cu-5Fe disc is different from the deformed texture at the same position, where the *C* component was replaced by A_1^* and *A* components leading to the formation of the partial *A*-fiber (presence of A_1^*/A_2^* and *A* components and absence of $\bar{A}$ component). It can be observed that the *B* component remains present and the shear texture components are more located at their ideal positions (see Figure 11b). From Figures 11d and 11f, it is evident that the textures at the mid-radius and edge positions were significantly changed after the annealing treatment. The *B* component disappeared, and it was replaced by a scattered A_2^* component, $\bar{A}$ and weak *C* and deviated A_1^* components. A complete *A*-fiber

(presence of $A/\bar{A}$ and A_1^*/A_2^* components) tends to form at the mid-radius position. The texture at the edge of the Cu-5Fe disc is quite similar to the mid-radius position, except for the absence of C component and strengthening of A_1^* component. Consequently, a full A-fiber is formed with the dominance of the A_2^* component.

3.4.2. Texture evolution of Fe grains

For statistical purposes, the texture of the Fe phase in the deformation and annealing conditions was analyzed only at the centre position (highest Fe fraction) and the results are presented in Figure 12 in terms of ODF sections at φ_2 = 0 and 45°. The positions of the ideal shear texture components for BCC materials are indicated in the ODF sections and their description in Miller indices ({hkl}<uvw>) and Euler angles (φ_1, Φ, φ_2) are summarized in Table 3 [46].

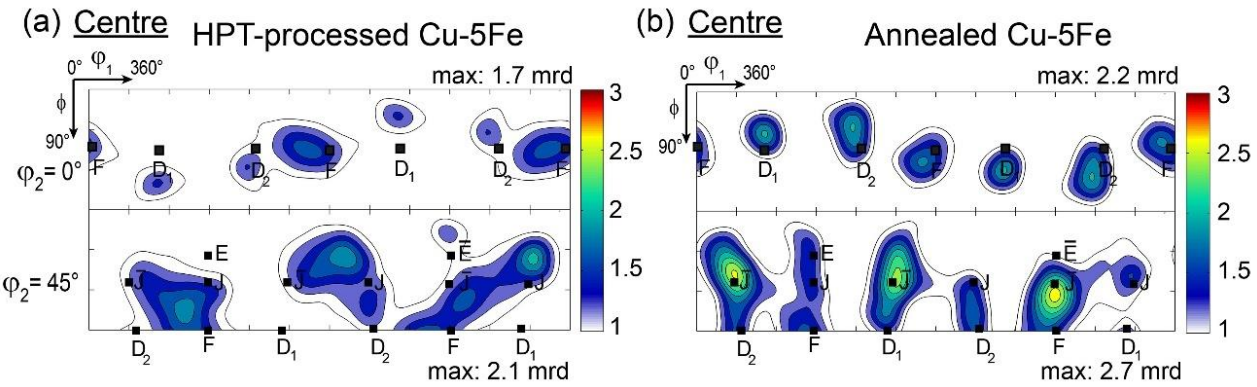

Figure 12: ODF sections at φ_2 = 0 and 45° showing the texture of Fe grains at the centre of: (a) HPT-processed and (b) annealed Cu-5Fe discs. The positions of the ideal shear texture components for BCC materials are indicated in the ODF sections.

The ODF sections in Figure 12a indicate the gradual formation of the typical shear texture of BCC materials with the formation of near F, J and $\bar{J}$ components. D_1 and D_2 components were also developed but with an obvious deviation from their ideal positions. Annealing at 500 °C for 6 h led to the formation of a typical shear texture where all shear components were present in their ideal positions and with a visible strengthening around the J and $\bar{J}$ components (see Figure 12b).

3.5.Mechanical properties

Figure 13 displays two-dimensional microhardness maps over the vertical cross-sections along the diameters of the HPT-processed and annealed Cu and Cu-5Fe discs, respectively. Before

HPT processing, the compacted Cu and Cu-5Fe discs exhibited average Vickers microhardness values of ~47.4 and ~48.8 Hv, respectively. For both HPT-processed discs (Figures 13a and 13c), the microhardness increases with increasing distance from the centre of the disc. For example, in the middle section, the microhardness at the centre of the HPT-processed Cu disc was found equal to 217 Hv and it increases to 233 and 238 Hv at the mid-radius and edge positions, respectively. For the HPT-processed Cu-5Fe disc, a value of 237 Hv was recorded at the centre position and it increases to 275 Hv at the mid-radius and then reaches a steady state after that (276 Hv at the edge position). Thus, it is evident that the Cu-5Fe disc is harder than the Cu disc.

The microhardness decreased after annealing treatment at 500 °C for 6 h (see Figure 13b) and becomes homogenously distributed across the Cu disc where an average value of 45 Hv is reached. While annealing at 500 °C for 6 h led to a softening in which the decrease in the microhardness is extended from the centre to the edge of the annealed Cu-5Fe disc (Figure 13d). For example, the value of microhardness at the centre, mid-radius and edge positions were about 135, 233 and 265 Hv, respectively. It is interesting to note that the decrease in the microhardness at the edge is small with respect to the deformed state at the same position (276 Hv).

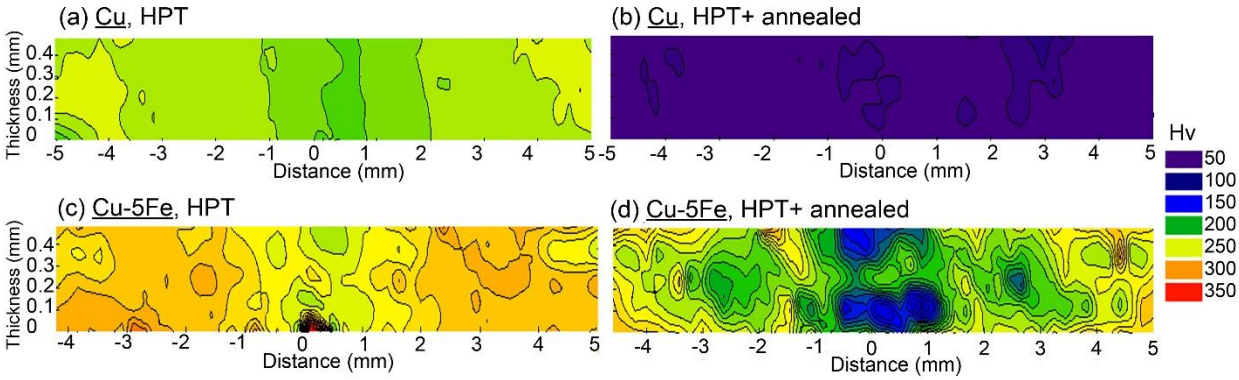

Figure 13: Hv mapping of HPT-processed and annealed: (a, b) Cu and (c, d) Cu-5Fe discs, respectively.

Based on the microhardness values, the deformation inhomogeneity can be accessed through the inhomogeneity factor, *IF*, using the following equation [47, 48]:

$$IF = \frac{\sqrt{\sum_{i=1}^{n}(Hv_i - Hv_{ave})^2/n-1}}{Hv_{ave}} \times 100 \quad (2)$$

where n is the number of microhardness measurements on each sample, Hv_{ave} is the average microhardness value, and Hv_i is the microhardness value of the i^{th} measurement. Basically, a

low *IF* value reflects a regular distribution of mechanical properties across the microstructure [48].

The values of *IF* for the HPT-processed and annealed Cu and Cu-5Fe discs are presented in Table 4. As can be noted, the HPT-processed Cu exhibits the lowest *IF* value (3.1%) and it increases significantly after annealing treatment (*IF* = 13.9%). For the Cu-5Fe disc, the highest value is recorded under HPT processing (*IF* = 20.7%) and then it decreases to 14.7% after the annealing treatment.

Table 4. IF values for the HPT- processed and annealed Cu and Cu-5Fe discs.

	HPT-processed Cu	Annealed Cu	HPT-processed Cu-5Fe	Annealed Cu-5Fe
IF (%)	3.1	13.9	20.7	14.7

Nevertheless, the observed hardness variations across the thickness of the HPT disc, which are especially pronounced after annealing, are attributed to the distinct shear patterns developed during HPT processing [49]. A greater shear strain near the disc surface promotes the earlier microstructural relaxation and this behavior is supported by recent studies: TEM analysis of HPT-processed Al-Mg alloys revealed enhanced solid-state mixing near the disk surfaces [50], Furthermore, XRD analysis showed an accelerated phase transformation near the disk surfaces which was more than the mid-thickness of nanostructured TiAl intermetallics [51], and in situ high-temperature laser-scanning confocal microscopy showed accelerated recovery at the surfaces of HPT-processed CoCrHeNiMn alloys [52].

4. Discussion

4.1. Deformation behaviour and texture evolution of consolidated discs

The experimental results concerning the deformation microstructures of the Cu and Cu-5Fe discs demonstrated that HPT processing at RT through 30 turns under an applied pressure of 6 GPa was effective for consolidation and mixing the immiscible Cu and Fe elements and provides the capability to form a bulk material with a nanocrystalline grain structure (Figures 4 and 5), a relatively large number of HAGBs (Figures 6b and d) and a shear-type texture (Figures 10 and 11). In addition, during the consolidation, CuO_2 oxide particles formed in the pure Cu disc and Fe grains and Fe_2O_3 oxide particles formed in the Cu-5Fe disc (see Figure 8). For both materials, the microstructural features, texture and microhardness evolution (Figures 13a and c) were dependent upon the distance from the centre of the disc. This is reasonable since the

equivalent strain, ε_{eq}, increases with increasing radial distance from the centre of the HPT-processed disc, as indicated by the following equation [53]:

$$\varepsilon_{eq} = \frac{2\pi Nr}{\sqrt{3}h} \quad (3)$$

where N is the number of HPT turn, r is the radial distance from the centre of the disc and h is the thickness of the disc. Accordingly, the equivalent strains calculated at the centre, mid-radius and edge positions were 36.2, 453.2 and 815.7, respectively.

In the majority of conventional bulk materials with medium to high stacking fault energies, such as Cu (~78 mJ/m^2) and Al (~160 mJ/m^2), the mean grain size decreased and the microhardness increased with increasing distance from the centre of the disc at low numbers of HPT turns due to the increase in shear strain (equation 3) and often a steady state across the disc is reached rapidly after 5 HPT turns which corresponds to the strain range of ε_{eq} ~ 6-150 [22, 46, 54]. Regarding the texture, the development of a shear texture is instable and gradually formed at low strain and then often stabilizes at the same strain level as the grain refinement [46]. Generally, the grain refinement during the HPT processing can be divided into the two stages of grain fragmentation and saturation [55]. In these materials, the deformation is accommodated by the activation of dislocation slip systems, their accumulation to form dislocation cell structure and then their gradual transformation into HAGBs with increasing shear strain to form new ultrafine or nano-sized grains through a continuous dynamic recrystallization (CDRX) mechanism [56]. A discontinuous dynamic recrystallization (DDRX) mechanism, which is characterized by the formation of recrystallized grains along the grain boundaries through nucleation and a growth process [56], can occurred concurrently with CDRX during the fragmentation stage [57].

According to these results, a homogeneity in grain refinement and microhardness evolution across the disc diameter in both consolidated Cu and Cu-5Fe discs was not reached even after 30 HPT turns ($\varepsilon_{eq} \approx$ 36.2- 815.7) and may require more HPT turns. Indeed, it was recently reported that HPT processing for 100 turns with an applied strain around ~3000 was required for obtaining a steady-state in the consolidated Cu-14Fe (wt.%) disc [31]. Thus, it is harder to achieve a complete saturation in the microstructure and microhardness in the consolidated powders than in conventional FCC bulk materials. In addition, the present results indicated that the deformation characteristics of the Cu and Cu-5Fe discs were different.

It is clear from the experimental data that the grain refinement and mechanical properties of the HPT-processed Cu disc failed to reach a steady-state condition across the disc diameter although

the texture was stable at the mid-radius and edge of the disc. In contrast, the HPT-processed Cu-5Fe disc appears to follow the deformation behaviour of HPT-processed bulk materials, where the mean grain size decreases and the microhardness increases from the centre to the mid-radius and saturates thereafter (ε_{eq} = 453.2). In addition, the texture was stable starting from the mid-radius of the disc.

In contrast to the HPT processing of bulk material, the shear deformation during HPT processing of powder particles plays two major roles [58-60]. At first, the continued shear deformation assures particle bonding and reduces the porosity. It is assumed that the substantial reduction in the particle size, high vacancy concentration and capillary pressures are the thermodynamic driving forces allowing the mechanical alloying of the Fe and Cu elements [27, 61]. Second, when the particle bonding is achieved, grain refinement is produced with further shear deformation. Thus, the microstructure and texture evolutions are expected to be different and more complicated than in the case of conventional bulk processed materials.

The results concerning the HPT-processed Cu disc indicate the development of high fractions of HAGBs (76%) and DRX (50.8%) at the centre position which mean the production of rapid grain refinement. This is supported by the formation of well-defined partial *B*-fiber and *A*-fiber textures. The drop in the fraction of HAGBs (62.2%) and DRX (39.1%) at the mid-radius position is explained by the occurrence of grain fragmentation. For a more detailed analysis, Figure 14 shows the enlarged zones of the microstructure at the centre, mid-radius and edge of the HPT processed Cu disc already presented in Figure 4 superposed with sub-grain boundaries, LAGBs and HAGBs in red, green and black colours, respectively.

As already noted, the microstructure at the centre of the disc contains a relatively low fraction of sub-grain boundaries and a very high fraction of HAGBs indicating the development of ultrafine grains through the DRX process. A high fraction of sub-grain boundaries (30.6%) is noticed in the mid-radius indicating a generation of new dislocations and this explains the increase in the stored energy (43.5 vs. 35.1 J/mol at the centre position). At this stage, the increase of dislocation density originates from the change in texture at the mid-radius position (see Figure 10c) which allows the activation of additional dislocation slip systems and their accumulation to form sub-grain boundaries. The change and the oscillation in the texture is mainly attributed to the amount of shear deformation and the heterogenous shear strain distribution due to the continuous rotation of the sample disc during the HPT processing [46, 62]. Based on equation 3, the equivalent strain at the centre position was low (ε_{eq} = 32.2) and it increases significantly at the mid-radius to ε_{eq} = 453.2 and at the edge to ε_{eq} = 815.7. This is

supported by the similar texture modification in the HPT-processed Cu-5Fe disc at the same strain level (Figure 11c).

In the blue boxes shown in Figure 14b there are some examples about the distribution of sub-grain boundaries within the grains. As shown in the elongated grain (G_1), the sub-grain boundaries are located inside the grains which increase the intragranular orientation spread and near the grain boundaries indicate the simultaneous triggering of the CDRX and DDRX mechanisms.

In the equiaxed blue grain (G_2), the sub-grain boundaries are only located near the grain boundaries showing the dominance of the DDRX mechanism. By contrast, in the purple grain (G_3) the distribution of sub-grains inside the grains is in the form of a straight line giving a typical fragmentation structure. By contrast, the green grain (G_4) is free from dislocations. These observations confirm the dependency of grain fragmentation on both grain orientation and grain size. Thus, not all grains go through the same level of plastic deformation at the same time and this may be another element influencing the texture modification over the disc diameter.

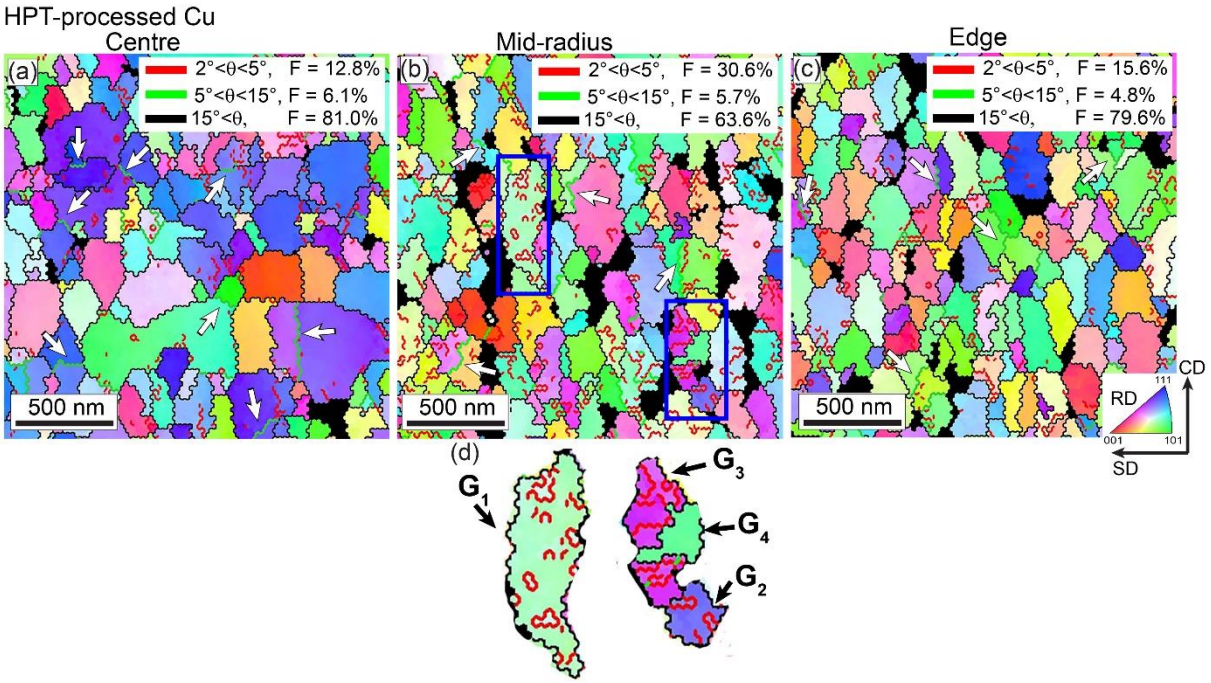

Figure 14: RD-IPF enlarged maps from Figure 4 superposed with grain boundary type at: (a) the centre, (b) mid-radius and (c) edge of the HPT-processed Cu disc, respectively. (d) G_1, G_2, G_3 and G_4 are examples to illustrate the dependency of sub-grains boundaries on the grain orientation.

The EBSD analysis shows that dislocations are the main deformation mode to accommodate the deformation under HPT processing. However, STEM observations (Figure 8) indicate the presence of deformed nano-twins in both the HPT-processed Cu and Cu-5Fe discs. It was found that the nanocrystalline copper promotes the formation of deformation twins during HPT processing at RT [63] and this was attributed to a partial dislocation emission from the grain boundaries [63]. It is well known that deformation twining is responsible for a texture transition during rolling of FCC materials with low stacking fault energy [64]. In the present study however, it is not possible to reach conclusions on the role of deformation nano-twins in the texture modification at the mid-radius and edge of the discs.

At the edge of the disc (see Figure 14c), the sub grain-boundaries decreased (15.6%) due to their continuous accumulation and their transformation into HAGBs (79.6%) thereby creating new nano-sized grains with a mean size (275 ± 30 nm) smaller than at the centre (200 ± 15 nm) of the disc. This is corroborated by the increase in the DRX fraction and the decrease in the stored energy as shown in Table 1. It is interesting to note that the fraction of LAGBs varied very little across the disc diameter (6.1, 5.7, 4.8% at the centre, mid-radius and edge positions, respectively). It is evident from the maps that the remaining LAGBs are mainly grain boundaries between grain neighbourhoods with similar orientations, as designated by white arrows in the three RD-IPF maps (Figure 14). Based on the latter observation, it is proposed that the consolidation of pure Cu powder by HPT processing through 30 turns undergoes two grain refinement stages. Thus, at the centre of the disc which corresponds to an equivalent strain of 36.2, the material already reached the saturation stage of the first grain refinement process. At the mid-radius where ε_{eq} = 453.2, the material is in the fragmentation stage of the second grain refinement process. Finally, at the edge of the disc (ε_{eq} = 815.7), the material reached the saturation stage of the second grain refinement process. It should be noted that the production of two grain refinement stages accompanied by two hardening stages was also reported in HPT processed aluminium-based alloys [57, 65].

During the second grain refinement regime, a partial *A*-fibre with a dominance of the A_2^* component developed (see Figures 10c and e) during the grain fragmentation and saturation stages. The development of an *A*-fiber texture was reported earlier in Cu-based alloys processed by HPT processing such as pure Cu [66], Cu/Ni layers [67] and a Cu-Ni-Si alloy [68].

Regarding the HPT-processed Cu-5Fe disc, the low DRX fraction and the high stored energy indicates that grain refinement rate was slower than for the HPT-processed Cu disc (see Table 1). Also, the development of a typical shear texture was restricted as is evident from the texture evolution at the centre of the HPT-processed disc (see Figure 11a). Moreover, the saturation in

the stored energy (44.7 J/mol) across the HPT-processed Cu-5Fe disc diameter suggests a balance between the generation and annihilation of dislocations where this evolution is a consequence of the addition of the Fe element which plays a major role as a solid solution element preventing dislocation movement and hence slowing the occurrence of the DRX process. This is supported by noting that the fraction of Fe grains (Figure 7) and their corresponding grain size (Table 2) decreased at the mid-radius and edge positions which means that the Fe grains were sheared and fragmented under the HPT processing and the Fe element dissolved in the Cu-matrix.

In addition, due to the difference in the intrinsic characteristics of the Cu and Fe grains, the creation of phase boundaries may play an important role in preventing dislocation movement and thereby inhibiting the DRX process and increasing the stored energy. The presence of Fe_2O_3 oxide particles as shown in the SEM (Figure 3) and STEM observations (Figure 8) could be also considered as a factor preventing the grain boundary mobility and dislocation motion. Consequently, the grain refinement becomes more effective (Figures 6a and c) and the structure is more strengthened, as shown by the microhardness values (Figure 13), in the Cu-5Fe disc than in the pure Cu disc. The restriction of DRX in the Cu-5Fe disc may indicate that the Fe element decreases the stacking fault energy of the fabricated composite to some extent. Based on the microstructural analysis, it may be reasonably assumed that the combination of grain boundaries, dislocations, second phase particles and solute strengthening contributed to the strain hardening of the Cu-5Fe disc.

It is noted that the texture modification from the centre towards the mid-radius position was not drastic (see Figures 11 a, c and e) when compared with the texture evolution of the HPT-processed Cu disc (see Figures 10 a, c and e). It could be connected to the inhibited DRX process due to the addition of Fe elements since it was reported that the phase boundaries can delay the texture formation because of the deformation accommodation between the two phases [69]. The dominance of $B/\bar{B}$ components with the presence of A_2^* or A_1^* components is frequently reported in materials with low stacking fault energies [46] which suggests that the Fe element may cause a decrease in the stacking fault energy of the Cu matrix.

The main characteristics of the deformation texture evolution in both consolidated discs are the deviations of the shear texture components from their ideal positions, especially at the mid-radius and edge positions. Moreover, it can be noted that the spread of some texture components like the A_2^* component in the HPT-processed Cu disc (see Figure 10) and B component in the HPT-processed Cu-5Fe disc (see Figure 11) may originate from the contribution of several causes simultaneously. Firstly, the deviation of shear texture components from their exact

positions is attributed to the convergent/divergent nature of the lattice rotation field around the ideal positions [59, 70]. Secondly, the HPT processing was performed under quasi-constrained conditions and thus it is expected that there is some lengthening of the processed disc which caused the shift of the preferred orientations towards the shear direction [71]. In addition, it is highly probable that, during the consolidation stage, the powder Cu and Fe particles have not been subjected to ideal shear deformation, leading to a deviation and the scattering of shear orientations [58].

4.2. Effect of annealing treatment on the consolidated discs

As expected, an annealing treatment at 500 °C for 6 h for the Cu and Cu-5Fe discs led to static recrystallization as manifest by grain growth (Figures 4-6) and decreasing microhardness values (Figures 13b and d). In addition to static recrystallization, the annealed Cu-5Fe disc exhibits the precipitation of the Fe phase as confirmed by the XRD pattern (Figure 2d), EBSD (see Figures 7d-f) and STEM (see Figure 9) results. However, the EBSD results suggest a dependency of static recrystallization behaviour on the measured position and the Fe element.

In the pure Cu disc, the annealed microstructure was reasonably similar across the disc diameter. The main microstructural characteristic of the annealed Cu disc is the presence of a high amount of Cu_2O oxide (see Figures 4d-f) which mainly originates from contamination during the consolidation process. This suggests that the densification of the Cu powder was not completely achieved and this was apparent only after the annealing treatment which caused damage to the microstructure and mechanical properties by reducing the HAGBs fraction (~55%) and an associated increase in the inhomogeneity factor (see Table 4). Thus, it is concluded that it would be preferable to conduct the annealing treatments of the consolidated pure Cu discs under a protective argon atmosphere to reduce the impact of oxygen.

The texture of the Cu disc after annealing was principally retained except for a weakening of *B*-fiber and the formation of *A* and A_2^* components at the centre position, as shown in Figures 10b, d and f. The occurrence of high DRX during deformation processing implies that all recrystallization nuclei exist already in the deformation state, as dynamically recrystallized grains or sub-grains, and the annealing treatment only provides the driving force for grain boundary migration. As a consequence, the deformation and recrystallization textures are similar. The development of a retained deformation texture is associated with the orientation growth theory [72, 73].

Regarding the annealed Cu-5Fe disc, the annealed microstructure (Figures 5d, e and f), texture (Figures 11b, d and f) and microhardness (Figure 13d) vary across the disc diameter. At the

centre and mid-radius positions, a duplex microstructure develops (see Figures 5d and e) due to the precipitation of Fe atoms from the Cu-rich matrix. Indeed, Figure 9 demonstrates that, unlike the fine grains, the coarse grains were free from the Fe element. Due to the limited solubility of the Fe element in the Cu matrix according to the Cu-Fe phase diagram [30], the annealing treatment increases the diffusion process of the Fe element leading to the nucleation and growth of Fe grains. In addition, the introduction of large numbers of crystalline defects such as dislocations and vacancies owing to the high shear strain serves to promote the phase transformation by creating additional diffusion paths. Consequently, on one hand the pinning effect in the Cu grains is no longer present which allows the mobility of grain boundaries to be increased. On the other hand, the presence of Fe_3O_2 particles with different sizes (see Figure 9) carried out sufficient pinning pressure to delay the grain boundary migration of the nano-sized grains. Despite the development of a heterogenous microstructure, the mechanical properties are more homogeneously distributed across the annealed disc diameter than in the HPT-processed disc, as demonstrated by the lowering of the *IF* factor after the annealing treatment (see Table 4). The improvement of the homogeneity could be attributed to the decrease of dislocation density and the formation of recrystalized grains. In fact, because of the heterogeneous nature of the microstructure (see Figure 5), it is possible that the annealed Cu-5Fe disc exhibits a good strength-ductility combination. It is excepted that the nano-sized grains provided the high strength while the elongation to failure would be supported through the coarse grains [16, 74].

Such heterogeneous microstructure is characteristic of an occurring discontinuous static recrystallization (DSRX), which includes the formation of nuclei of recrystallized grains and their consequent fast growth by grain boundary migration. This is known to follow the oriented nucleation theory [72, 73]. Usually, the occurrence of the DSRX mechanism in conventional deformed materials is accompanied by a noticeable change in the annealed texture [75, 76] which is in good agreement with the texture change observed at the centre and mid-radius positions (see Figure 11). It is interesting to note that the texture modification after annealing occurred also in the Fe grains, as can be shown in Figure 12. The strengthening of $J/\bar{J}$ components was reported in an HPT-processed and annealed Fe-9Cr (wt.%) alloy [77]. It was demonstrated that the $J/\bar{J}$ oriented grains exhibit high stored energy and were surrounded by special grain boundaries which favour their recrystallization and their grain growth [77]. The coarse Cu grains at the mid-radius position were decorated by a high fraction of annealing twins (see Figure 5e) which may be considered as an additional source for the texture modification.

To confirm this proposal. Figure 15 shows an example of the RD-IPF maps superimposed with HAGBs (black line) and twin boundaries (red line) of nano-sized and coarse Cu grains taken from the mid-radius position of the annealed Cu-5Fe disc (the RD-IPF map shown in Figure 5e). First, the fraction of twins in the nano-sized grains is very low and they form a straight line (see white arrows) like a random grain boundary. The orientation of the nano-sized grains is dominated by the A_2^* component as demonstrated by the corresponding {111} pole figure.

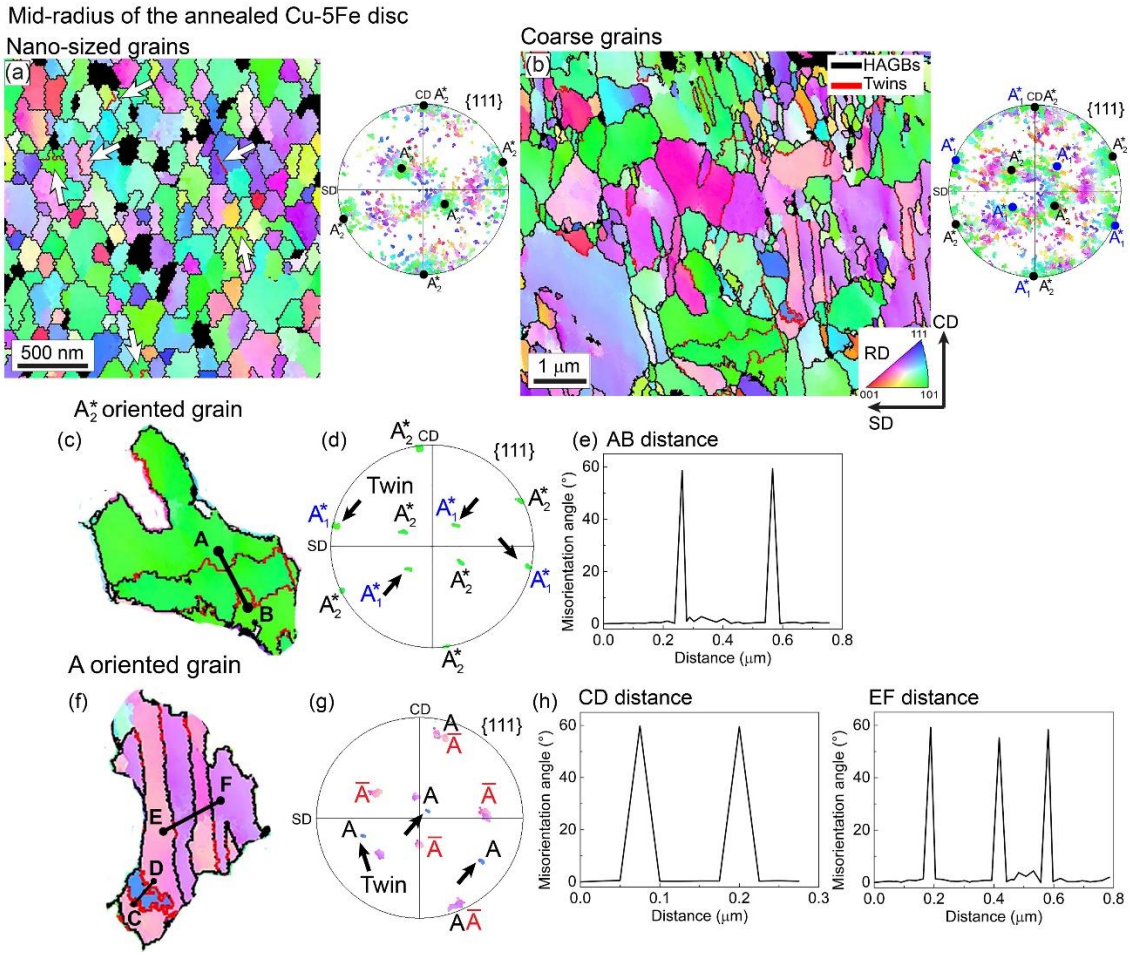

Figure 15: RD-IPF maps superposed with HAGBs and annealed twin boundaries and corresponding {111} pole figures of: (a) nano-sized and (b) coarse grains taken from the mid-radius position of the annealed Cu-5Fe disc (Figure 5e). (c, f) example of A_2^* and A oriented grains, (d, g) {111} pole figures showing the orientation relationship between the parent A_2^* and A oriented grains and the twined regions and (e, h) misorientation profiles corresponding to the AB distance in the A_2^* oriented grain, and CD and EF distances in the A oriented grain, respectively.

By contrast, the fraction of annealing twins is visibly high in the coarse grains and exhibits a lamellar and band form. According to the corresponding {111} pole figure, the texture of these coarse grains is dominated by the A_2^* and A_1^* orientations.

In Figures 15c and 15f, the isolated parent A_2^* and A oriented grains contain typical twin Σ3 (60°<111>) as demonstrated by the profile misorientation along the AB (see Figure 15e) and CD (see Figure 15h) distances, respectively. The isolated A oriented grain contains also several twins in the form of steps, as can be seen from the profile misorientation along the EF distance (see Figure 15h).

The corresponding {111} pole figure reveals the crystallographic relationship between the parent A_2^* (Figure 15d) and A (Figure 15g) oriented grains and the twinned area. It is clear that the twining in the A_2^* and A oriented grains led to the formation of A_1^* and $\bar{A}$ orientations, respectively, which explains their strengthening at the mid-radius position after the annealing treatment.

It is expected that the annealed microstructure at the mid-radius and edge positions will be similar since the average deformed grain size (Figure 6c), the deformation texture (Figures 11c and e), the microhardness (Figure 13 c) and the stored energy (Table 1) were similar. However, the present results demonstrate a good thermal stability of the edge position but with a net change in the texture evolution (see Figures 5c and f). The uniform grain distribution after the annealing treatment is often associated with the continuous static recrystallization (CSRX) mechanism [78]. The CSRX mechanism applied the continuous transformation of sub-grains boundaries and LAGBs into HAGBs and this allows the production of a homogeneous microstructural evolution [78]. As shown in Figure 6d, the fraction of HAGBs at the edge position was not changed after annealing (67% under deformation state vs. 65% under annealing state) since the HAGBs already formed during the HPT processing owing to the grain refinement. It is recognized that the transition from the DSRX to the CSRX mechanism is controlled by several parameters such as second particles, large strain and the critical fraction of HAGBs [75, 76, 79]. Based on the current microstructural evolution, the transition from the DSRX to the CSRX mechanism can be attributed to the difference in distribution and size of the Fe phase at the mid-radius and edge positions. Although the fraction of the Fe phase is similar (~4.0%), it is apparent that the Fe grains at the edge position are more refined (Table 2) and homogenously dispersed (Figure 7) within the microstructure. Therefore, it is expected that the Cu/Fe grain interfaces delay the expansion of the two-phase grain boundaries which eventually prevent the grain growth of both the Fe and Cu grains.

In addition, the equivalent strain at the edge position (ε_{eq} = 815.7) is almost ~2 times higher than in the mid-radius (ε_{eq} = 453.2) position which increases the fraction of HAGBs from 61% to 67% leading to a more stable microstructure. This critical HAGBs value is consistent with previous investigations where it was found that the DSRX mechanism type dominated when the HAGBs fraction was less than 62% and the CSRX mechanism type was dominant if the HAGBs fraction was larger than 64% [75, 79]. Therefore, it is anticipated that it is necessary to obtain a deformation microstructure consisting of nano-sized grains with an HAGBs fraction of 67% in order to convert the annealed duplex microstructure into a uniform grain distribution. Furthermore, the transition from the DSRX to the CDRX mechanism has a great impact on the annealed grain size (see Figure 6c) but it appears to have little effect on the annealed texture evolution since at both positions the deformation texture changes into a complete *A*-fiber (see Figures 11d and 11f). Generally, the deformation texture is retained during the occurrence of the CSRX mechanism [75, 76]. In the current research, regardless of the occurrence of the DSRX or CRSX mechanism, the texture change after annealing at both positions is a result of the restricted DRX and may be interpreted based on the oriented nucleation theory where the recrystallized texture arises from those nuclei which have the fastest growth rate in the deformed state [72].

A significant result is that the deformation textures in both the pure Cu and Cu-5Fe materials were different but ultimately they had similar textures after the annealing treatment. The partial *A*-fiber (A_1^*/A_2^* and A components with the absence of $\bar{A}$ component) was developed during deformation processing in the Cu disc through DRX and this was retained after the annealing treatment. For the Cu-5Fe disc, the complete *A*-fiber (A_1^*/A_2^* and $A/\bar{A}$ components) was developed only after annealing due to the restriction of the DRX process. Eventually, it can be concluded that the *A*-fiber is a stable texture in the consolidated Cu and Cu-5Fe discs. Nevertheless, some differences are noticed such as the development of the $\bar{A}$ component and the strengthening of the annealed texture mainly due to the effect of the Fe addition (see Figures 11d and f). Finally, it is noted that the results demonstrate that the consolidated Cu-5Fe disc has a better thermal stability than the pure Cu disc.

5. Conclusions

The current investigation provides valuable insights into the deformation and static recrystallization behaviours of consolidated pure Cu and Cu-5Fe discs fabricated by HPT processing at RT through 30 turns. The main conclusions are as follows:

For the HPT-processed Cu disc, two grain refinement regimes were evident due to the accelerated DRX process leading to a grain size around 230 ± 15 nm and the formation of a partial *A*-fiber (A_1^*/A_2^* and *A* components with the absence of $\bar{A}$ component). The formation of Cu_2O particles caused a serious oxidation problem during the annealing treatment, which inevitably affected the performance of the consolidated Cu disc. Despite this, the partial *A*-fiber persists after the annealing treatment.

For the HPT-processed Cu-5Fe disc, the DRX process was restricted so that there was more grain refinement (around 190 ± 20 nm) and a gradual shear texture formation in both the Cu and Fe grains. The CDRX and DDRX mechanisms simultaneously govern the grain refinement. The microhardness increased from the centre to the edge of the processed disc which caused a heterogenous distribution of the mechanical properties. The HAGBs fraction and the precipitation of the Fe phase and its distribution during annealing treatment are responsible for the duplex microstructures at the centre and mid-radius positions and the stable microstructure at the edge position, respectively. Consequently, the transition from the DSRX to the CSRX mechanism was apparent across the annealed disc diameter. The presence of Fe_2O_3 oxide particles contributed to prevent grain growth. The restricted DRX process and annealing twins were responsible for the development of a recrystallization texture consisting of complete *A*-fiber (presence of A_1^*/A_2^* and $A/\bar{A}$ components). The microhardness decreased due to the softening process and it was more homogeneously distributed across the disc diameter than the HPT-processed disc.

Acknowledgements

This research was partially supported by the PHC-Tassili program No. 24MDU114. National Science Centre Poland provided funding for Dr P. Bazarnik under Grant Agreement No UMO-2024/53/B/ST11/00531.

Conflict of Interest: The authors declare no conflict of interest.

Data and code availability: The datasets generated during the experiments and analyzed under the current study are available from the corresponding authors upon reasonable request.

Supplementary information: N/A

Ethical approval: The authors have adhered to the accepted ethical standards of a genuine research study.

References

[1] Y. Wu, W. Zhang, Y. Li, F. Yang, H. Liu, J. Zou, J. Jiang, F. Fang, A. Ma, An overview of microstructure regulation treatment of Cu-Fe alloys to improve strength, conductivity, and electromagnetic shielding, Journal of Alloys and Compounds 1002 (2024) 175425.
[2] C.P. Wang, X.J. Liu, R. Kainuma, Y. Takaku, I. Ohnuma, K. Ishida, Formation of core-type macroscopic morphologies in Cu-Fe base alloys with liquid miscibility gap, Metallurgical and Materials Transactions A 35(4) (2004) 1243-1253.
[3] M. Wang, Q.-r. Yang, Y.-b. Jiang, Z. Li, Z. Xiao, S. Gong, Y.-r. Wang, C.-l. Guo, H.-g. Wei, Effects of Fe content on microstructure and properties of Cu–Fe alloy, Transactions of Nonferrous Metals Society of China 31(10) (2021) 3039-3049.
[4] S.B. Luo, W.L. Wang, J. Chang, Z.C. Xia, B. Wei, A comparative study of dendritic growth within undercooled liquid pure Fe and Fe50Cu50 alloy, Acta Materialia 69 (2014) 355-364.
[5] M. Guo, F. Wang, L. Yi, The microstructure controlling and deformation behaviors of Cu–Fe–C alloy prepared by rapid solidification, Materials Science and Engineering: A 657 (2016) 197-209.
[6] C. Zhang, C. Chen, P. Li, M. Yan, Q. Qin, F. Yang, W. Wang, Z. Guo, A.A. Volinsky, Microstructure and properties evolution of rolled powder metallurgy Cu-30Fe alloy, Journal of Alloys and Compounds 909 (2022) 164761.
[7] K.M. Liu, D.P. Lu, H.T. Zhou, S.F. Wen, S.Y. Wei, Q. Hu, Z.Z. Wan, Microstructure and Properties of Cu-17Fe Alloy Aged Treatment in High Magnetic Field, Advanced Materials Research 194-196 (2011) 1270-1274.
[8] H.R. Jo, J.T. Kim, S.H. Hong, Y.S. Kim, H.J. Park, W.J. Park, J.M. Park, K.B. Kim, Effect of silicon on microstructure and mechanical properties of Cu-Fe alloys, Journal of Alloys and Compounds 707 (2017) 184-188.
[9] Y.B. Jeong, H.R. Jo, H.J. Park, H. Kato, K.B. Kim, Mechanical properties and microstructural change in (Cu–Fe) immiscible metal matrix composite: Effect of Mg on secondary phase separation, Journal of Materials Research and Technology 9(6) (2020) 15989-15995.
[10] P. Zhang, Q. Lei, X. Yuan, X. Sheng, D. Jiang, Y. Li, Z. Li, Microstructure and mechanical properties of a Cu-Fe-Nb alloy with a high product of the strength times the elongation, Materials Today Communications 25 (2020) 101353.
[11] D. Yuan, Z. Liu, C. Guo, H. Zeng, J. Zhang, M. Li, B. Peng, B. Yang, Effect of In on Fe phase morphology and properties of Cu-Fe alloy, Materials Science and Technology 39(18) (2023) 3278-3287.
[12] H. Zhang, H. Zhang, L. Li, Hot deformation behavior of Cu–Fe–P alloys during compression at elevated temperatures, Journal of Materials Processing Technology 209(6) (2009) 2892-2896.
[13] Q. Dong, L. Shen, F. Cao, Y. Jia, K. Liao, M. Wang, Effect of Thermomechanical Processing on the Microstructure and Properties of a Cu-Fe-P Alloy, Journal of Materials Engineering and Performance 24(4) (2015) 1531-1539.
[14] M. Wang, Y. Jiang, Z. Li, Z. Xiao, S. Gong, W. Qiu, Q. Lei, Microstructure evolution and deformation behaviour of Cu-10 wt%Fe alloy during cold rolling, Materials Science and Engineering: A 801 (2021) 140379.
[15] C. Zhang, C. Chen, L. Huang, T. Lu, P. Li, W. Wang, F. Yang, A.A. Volinsky, Z. Guo, Microstructure and properties of Cu-Fe alloys fabricated via powder metallurgy and rolling, Powder Metallurgy 64(4) (2021) 308-320.
[16] J. Xu, B. Guan, R. Fu, Y. Wu, Q. Hu, J. Zou, G. Huang, C. Yan, Tailoring the microstructure and mechanical properties of Cu–Fe alloy by varying the rolling path and rolling temperature, Journal of Materials Research and Technology 27 (2023) 182-193.

[17] Y.Z. Tian, Y. Yang, S.Y. Peng, X.Y. Pang, S. Li, M. Jiang, H.X. Li, J.W. Wang, G.W. Qin, Managing mechanical and electrical properties of nanostructured Cu-Fe composite by aging treatment, Materials Characterization 196 (2023) 112600.
[18] J. Xu, B. Guan, R. Fu, J. Huang, W. Liu, Q. Hu, Z. Hu, C. Yan, The effect of multi-directional compression on mechanical properties and corrosion properties of Cu–Fe composite, Journal of Materials Research and Technology 28 (2024) 1497-1503.
[19] D.-P. Lu, J. Wang, W.-J. Zeng, Y. Liu, L. Lu, B.-D. Sun, Study on high-strength and high-conductivity Cu–Fe–P alloys, Materials Science and Engineering: A 421(1) (2006) 254-259.
[20] K. Edalati, A. Bachmaier, V.A. Beloshenko, Y. Beygelzimer, V.D. Blank, W.J. Botta, K. Bryła, J. Čížek, S. Divinski, N.A. Enikeev, Y. Estrin, G. Faraji, R.B. Figueiredo, M. Fuji, T. Furuta, T. Grosdidier, J. Gubicza, A. Hohenwarter, Z. Horita, J. Huot, Y. Ikoma, M. Janeček, M. Kawasaki, P. Král, S. Kuramoto, T.G. Langdon, D.R. Leiva, V.I. Levitas, A. Mazilkin, M. Mito, H. Miyamoto, T. Nishizaki, R. Pippan, V.V. Popov, E.N. Popova, G. Purcek, O. Renk, Á. Révész, X. Sauvage, V. Sklenicka, W. Skrotzki, B.B. Straumal, S. Suwas, L.S. Toth, N. Tsuji, R.Z. Valiev, G. Wilde, M.J. Zehetbauer, X. Zhu, Nanomaterials by severe plastic deformation: review of historical developments and recent advances, Materials Research Letters 10(4) (2022) 163-256.
[21] A.P. Zhilyaev, T.G. Langdon, Using high-pressure torsion for metal processing: Fundamentals and applications, Progress in Materials Science 53(6) (2008) 893-979.
[22] K. Edalati, A.Q. Ahmed, S. Akrami, K. Ameyama, V. Aptukov, R.N. Asfandiyarov, M. Ashida, V. Astanin, A. Bachmaier, V. Beloshenko, E.V. Bobruk, K. Bryła, J.M. Cabrera, A.P. Carvalho, N.Q. Chinh, I.-C. Choi, R. Chulist, J.M. Cubero-Sesin, G. Davdian, M. Demirtas, S. Divinski, K. Durst, J. Dvorak, P. Edalati, S. Emura, N.A. Enikeev, G. Faraji, R.B. Figueiredo, R. Floriano, M. Fouladvind, D. Fruchart, M. Fuji, H. Fujiwara, M. Gajdics, D. Gheorghe, Ł. Gondek, J.E. González-Hernández, A. Gornakova, T. Grosdidier, J. Gubicza, D. Gunderov, L. He, O.F. Higuera, S. Hirosawa, A. Hohenwarter, Z. Horita, J. Horky, Y. Huang, J. Huot, Y. Ikoma, T. Ishihara, Y. Ivanisenko, J.-i. Jang, A.M. Jorge, M. Kawabata-Ota, M. Kawasaki, T. Khelfa, J. Kobayashi, L. Kommel, A. Korneva, P. Kral, N. Kudriashova, S. Kuramoto, T.G. Langdon, D.-H. Lee, V.I. Levitas, C. Li, H.-W. Li, Y. Li, Z. Li, H.-J. Lin, K.-D. Liss, Y. Liu, D.M.M. Cardona, K. Matsuda, A. Mazilkin, Y. Mine, H. Miyamoto, S.-C. Moon, T. Müller, J.A. Muñoz, M.Y. Murashkin, M. Naeem, M. Novelli, D. Olasz, R. Pippan, V.V. Popov, E.N. Popova, G. Purcek, P. de Rango, O. Renk, D. Retraint, Á. Révész, V. Roche, P. Rodriguez-Calvillo, L. Romero-Resendiz, X. Sauvage, T. Sawaguchi, H. Sena, H. Shahmir, X. Shi, V. Sklenicka, W. Skrotzki, N. Skryabina, F. Staab, B. Straumal, Z. Sun, M. Szczerba, Y. Takizawa, Y. Tang, R.Z. Valiev, A. Vozniak, A. Voznyak, B. Wang, J.T. Wang, G. Wilde, F. Zhang, M. Zhang, P. Zhang, J. Zhou, X. Zhu, Y.T. Zhu, Severe plastic deformation for producing superfunctional ultrafine-grained and heterostructured materials: An interdisciplinary review, Journal of Alloys and Compounds 1002 (2024) 174667.
[23] K. Edalati, Z. Horita, Application of high-pressure torsion for consolidation of ceramic powders, Scripta Materialia 63(2) (2010) 174-177.
[24] A. Bachmaier, R. Pippan, High-Pressure Torsion Deformation Induced Phase Transformations and Formations: New Material Combinations and Advanced Properties, Materials Transactions 60(7) (2019) 1256-1269.
[25] J.-K. Han, T. Herndon, J.-i. Jang, T.G. Langdon, M. Kawasaki, Synthesis of Hybrid Nanocrystalline Alloys by Mechanical Bonding through High-Pressure Torsion, Advanced Engineering Materials 22(4) (2020) 1901289.
[26] D. Hernández-Escobar, M. Kawasaki, C.J. Boehlert, Metal hybrids processed by high-pressure torsion: synthesis, microstructure, mechanical properties and developing trends, International Materials Reviews 67(3) (2022) 231-265.

[27] X. Sauvage, F. Wetscher, P. Pareige, Mechanical alloying of Cu and Fe induced by severe plastic deformation of a Cu–Fe composite, Acta Materialia 53(7) (2005) 2127-2135.
[28] A. Bachmaier, R. Pippan, Microstructure and Properties of a Fe-Cu Composite Processed by HPT Powder Consolidation, Materials Science Forum 667-669 (2011) 229-234.
[29] A. Bachmaier, M. Kerber, D. Setman, R. Pippan, The formation of supersaturated solid solutions in Fe–Cu alloys deformed by high-pressure torsion, Acta Materialia 60(3) (2012) 860-871.
[30] A. Lukyanov, A. Churakova, D. Gunderov, A. Filatov, E. Antipov, V. Sitdikov, A. Ganeev, R. Valiev, V.J.R.A.M.S. Pushin, Microstructure transformation in a cast Cu-Fe alloy at high pressure torsion deformation, Rev. Adv. Mater. Sci. 45(1-2) (2016) 20-27.
[31] M. Stückler, H. Krenn, P. Kürnsteiner, B. Gault, F. De Geuser, L. Weissitsch, S. Wurster, R. Pippan, A. Bachmaier, Intermixing of Fe and Cu on the atomic scale by high-pressure torsion as revealed by DC- and AC-SQUID susceptometry and atom probe tomography, Acta Materialia 196 (2020) 210-219.
[32] P. Asghari-Rad, Y.T. Choi, N.T.-C. Nguyen, P. Sathiyamoorthi, H.S. Kim, Fabrication of Layered Cu-Fe-Cu Structure by Cold Consolidation of Powders using High-pressure Torsion, J Korean Powder Metall Inst 28(4) (2021) 287-292.
[33] M. Liu, R. Zheng, H. Li, Q. Wei, C. Ma, N. Tsuji, Phase decomposition behavior and its impact on mechanical properties in bulk nanostructured Cu-20 at.%Fe supersaturated solid solution, Journal of Materials Science & Technology 185 (2024) 207-220.
[34] R.B. Figueiredo, P.R. Cetlin, T.G. Langdon, Using finite element modeling to examine the flow processes in quasi-constrained high-pressure torsion, Materials Science and Engineering: A 528(28) (2011) 8198-8204.
[35] K. Edalati, Z. Horita, T.G. Langdon, The significance of slippage in processing by high-pressure torsion, Scripta Materialia 60(1) (2009) 9-12.
[36] K. Edalati, Y. Hashiguchi, P.H.R. Pereira, Z. Horita, T.G. Langdon, Effect of temperature rise on microstructural evolution during high-pressure torsion, Materials Science and Engineering: A 714 (2018) 167-171.
[37] Y. Huang, S. Sabbaghianrad, A.I. Almazrouee, K.J. Al-Fadhalah, S.N. Alhajeri, T.G. Langdon, The significance of self-annealing at room temperature in high purity copper processed by high-pressure torsion, Materials Science and Engineering: A 656 (2016) 55-66.
[38] J.-H. Cho, A.D. Rollett, K.H. Oh, Determination of a mean orientation in electron backscatter diffraction measurements, Metallurgical and Materials Transactions A 36(12) (2005) 3427-3438.
[39] H. Azzeddine, T. Baudin, A.-L. Helbert, F. Brisset, Y. Huang, M. Kawasaki, D. Bradai, T.G. Langdon, A stored energy analysis of grains with shear texture orientations in Cu-Ni-Si and Fe-Ni alloys processed by high-pressure torsion, Journal of Alloys and Compounds 864 (2021) 158142.
[40] Y. Takayama, J.A. Szpunar, H. Kato, Analysis of Intragranular Misorientation Related to Deformation in an Al-Mg-Mn Alloy, Materials Science Forum 495-497 (2005) 1049-1054.
[41] R. Hielscher, H. Schaeben, A novel pole figure inversion method: specification of the MTEX algorithm, Journal of Applied Crystallography 41(6) (2008) 1024-1037.
[42] M. Andrzejczuk, J. Siejka-Kulczyk, M. Lewandowska, K.J. KurzydŁOwski, Microstructure investigations of dental composite samples prepared by focused ion beam technique, Journal of Microscopy 237(3) (2010) 427-430.
[43] H. Azzeddine, B.Y. Islem, K.A. Yazid, B. Thierry, H. Anne-Laure, B. François, K. Megumi, B. Djamel, T.G. and Langdon, An investigation of the stored energy and thermal stability in a Cu–Ni–Si alloy processed by high-pressure torsion, Philosophical Magazine 100(6) (2020) 688-712.

[44] I. Lee, L. Bhatta, D. Xu, M. Blankenburg, U. Lienert, K.-D. Liss, M. Kawasaki, Defect-driven relaxation of nanostructured Cu examined by in situ heating high-energy synchrotron X-ray microbeam diffraction, Journal of Alloys and Compounds 1028 (2025) 180599.
[45] J. Wongsa-Ngam, M. Kawasaki, T.G. Langdon, A comparison of microstructures and mechanical properties in a Cu–Zr alloy processed using different SPD techniques, Journal of Materials Science 48(13) (2013) 4653-4660.
[46] H. Azzeddine, D. Bradai, T. Baudin, T.G. Langdon, Texture evolution in high-pressure torsion processing, Progress in Materials Science 125 (2022) 100886.
[47] S. Sadi, A. Hanna, H. Azzeddine, C. Casas, T. Baudin, A.-L. Helbert, F. Brisset, J.M. Cabrera, Characterization of microstructure and texture of binary Mg-Ce alloy processed by equal channel angular pressing, Materials Characterization 181 (2021) 111454.
[48] E. Rafizadeh, A. Mani, M. Kazeminezhad, The effects of intermediate and post-annealing phenomena on the mechanical properties and microstructure of constrained groove pressed copper sheet, Materials Science and Engineering: A 515(1) (2009) 162-168.
[49] R. Kulagin, Y. Beygelzimer, Y. Ivanisenko, A. Mazilkin, H. Hahn, High Pressure Torsion: from Laminar Flow to Turbulence, IOP Conference Series: Materials Science and Engineering 194(1) (2017) 012045.
[50] Y.-H. Wu, L. Bhatta, I. Lee, R.B. Figueiredo, M. Kawasaki, M.K. Santala, Multi-scale Characterization of Supersaturated and Intermetallic Nanoscale Phases in Alloys Produced by High-Pressure Torsion Processing of Al and Mg Sheets, JOM 77(3) (2025) 1233-1240.
[51] X. Li, R.J. Dippenaar, J.-K. Han, M. Kawasaki, K.-D. Liss, Phase transformation and structure evolution of a Ti-45Al-7.5Nb alloy processed by high-pressure torsion, Journal of Alloys and Compounds 787 (2019) 1149-1157.
[52] M. Kawasaki, J.-K. Han, X. Liu, S.-C. Moon, K.-D. Liss, Synchrotron High-Energy X-ray & Neutron Diffraction, and Laser-Scanning Confocal Microscopy: In-Situ Characterization Techniques for Bulk Nanocrystalline Metals, Materials Transactions 64(8) (2023) 1683-1694.
[53] F. Wetscher, A. Vorhauer, R. Stock, R. Pippan, Structural refinement of low alloyed steels during severe plastic deformation, Materials Science and Engineering: A 387-389 (2004) 809-816.
[54] O. Renk, R. Pippan, Saturation of Grain Refinement during Severe Plastic Deformation of Single Phase Materials: Reconsiderations, Current Status and Open Questions, Materials Transactions 60(7) (2019) 1270-1282.
[55] R. Pippan, S. Scheriau, A. Taylor, M. Hafok, A. Hohenwarter, A. Bachmaier, Saturation of Fragmentation During Severe Plastic Deformation, Annual Review of Materials Research 40 (2010) 319-343.
[56] T. Sakai, A. Belyakov, R. Kaibyshev, H. Miura, J.J. Jonas, Dynamic and post-dynamic recrystallization under hot, cold and severe plastic deformation conditions, Progress in Materials Science 60 (2014) 130-207.
[57] A. Khalfallah, H. Azzeddine, T. Baudin, F. Brisset, Y. Huang, T.G. Langdon, Texture and microstructural evolution in an Al-6061 alloy processed by high-pressure torsion, Materials Characterization 212 (2024) 114020.
[58] S. Panda, L.S. Toth, J. Zou, T. Grosdidier, Effect of Strain Heterogeneities on Microstructure, Texture, Hardness, and H-Activation of High-Pressure Torsion Mg Consolidated from Different Powders, Materials, 2018.
[59] Y. Zhao, R. Massion, T. Grosdidier, L.S. Toth, Gradient Structure in High Pressure Torsion Compacted Iron Powder, Advanced Engineering Materials 17(12) (2015) 1748-1753.
[60] Y.J. Zhao, R. Massion, T. Grosdidier, L.S. Toth, Contribution of shear deformation to grain refinement and densification of iron powder consolidated by high pressure torsion, IOP Conference Series: Materials Science and Engineering 63(1) (2014) 012032.

[61] A.R. Yavari, P.J. Desré, T. Benameur, Mechanically driven alloying of immiscible elements, Physical Review Letters 68(14) (1992) 2235-2238.
[62] L.S. Tóth, K.W. Neale, J.J. Jonas, Stress response and persistence characteristics of the ideal orientations of shear textures, Acta Metallurgica 37(8) (1989) 2197-2210.
[63] X.Z. Liao, Y.H. Zhao, S.G. Srinivasan, Y.T. Zhu, R.Z. Valiev, D.V. Gunderov, Deformation twinning in nanocrystalline copper at room temperature and low strain rate, Applied Physics Letters 84(4) (2004) 592-594.
[64] W. Heye, G. Wasserman, The formation of the rolling textures in FCC metals by slip and twinning, Scripta Metallurgica 2(4) (1968) 205-207.
[65] I.C. dos Santos, E.M. Mazzer, R.B. Figueiredo, T.G. Langdon, P.H.R. Pereira, Evidence for two-stage hardening in an Al-Zn-Mg-Cu alloy processed by high-pressure torsion, Journal of Alloys and Compounds 941 (2023) 168839.
[66] K.J. Al-Fadhalah, S.N. Alhajeri, A.I. Almazrouee, T.G. Langdon, Microstructure and microtexture in pure copper processed by high-pressure torsion, Journal of Materials Science 48(13) (2013) 4563-4572.
[67] E.H. Ekiz, T.G. Lach, R.S. Averback, N.A. Mara, I.J. Beyerlein, M. Pouryazdan, H. Hahn, P. Bellon, Microstructural evolution of nanolayered Cu–Nb composites subjected to high-pressure torsion, Acta Materialia 72 (2014) 178-191.
[68] A.Y. Khereddine, F. Hadj Larbi, H. Azzeddine, T. Baudin, F. Brisset, A.-L. Helbert, M.-H. Mathon, M. Kawasaki, D. Bradai, T.G. Langdon, Microstructures and textures of a Cu–Ni–Si alloy processed by high-pressure torsion, Journal of Alloys and Compounds 574 (2013) 361-367.
[69] J. Xu, Y. Peng, B. Guan, Y. Xin, A. Chapuis, G. Huang, Q. Liu, Tailoring the microstructure and texture of a dual-phase Mg–8Li alloy by varying the rolling path, Materials Science and Engineering: A 844 (2022) 143202.
[70] J. Baczynski, J.J. Jonas, Texture development during the torsion testing of α-iron and two IF steels, Acta Materialia 44(11) (1996) 4273-4288.
[71] I.J. Beyerlein, L.S. Tóth, Texture evolution in equal-channel angular extrusion, Progress in Materials Science 54(4) (2009) 427-510.
[72] R.D. Doherty, Nucleation and growth kinetics of different recrystallization texture components, Scripta Metallurgica 19(8) (1985) 927-930.
[73] U. Schmidt, K. Lücke, Recrystallization Textures of Silver, Copper and α-Brasses With Different Zinc-Contents as a Function of the Rolling Temperature, Texture, Stress, and Microstructure 3(2) (1979) 146381.
[74] Z. Cheng, L. Bu, Y. Zhang, H. Wu, T. Zhu, L. Lu, Characterization of gradient plastic deformation in gradient nanotwinned Cu, Acta Materialia 246 (2023) 118673.
[75] H. Jazaeri, F.J. Humphreys, The transition from discontinuous to continuous recrystallization in some aluminium alloys: II – annealing behaviour, Acta Materialia 52(11) (2004) 3251-3262.
[76] H. Jazaeri, F.J. Humphreys, The transition from discontinuous to continuous recrystallization in some aluminium alloys: I – the deformed state, Acta Materialia 52(11) (2004) 3239-3250.
[77] J. Duan, H. Wen, C. Zhou, R. Islamgaliev, X. Li, Evolution of microstructure and texture during annealing in a high-pressure torsion processed Fe-9Cr alloy, Materialia 6 (2019) 100349.
[78] R.D. Doherty, D.A. Hughes, F.J. Humphreys, J.J. Jonas, D.J. Jensen, M.E. Kassner, W.E. King, T.R. McNelley, H.J. McQueen, A.D. Rollett, Current issues in recrystallization: a review, Materials Science and Engineering: A 238(2) (1997) 219-274.
[79] M.F. Ashby, F.J. Humphreys, C.M. Sellar, H.R. Shercliff, M.J. Stowell, F.J. Humphreys, P.B. Prangnell, J.R. Bowen, A. Gholinia, C. Harris, Developing stable fine–grain microstructures by large strain deformation, Philosophical Transactions of the Royal Society of

London. Series A: Mathematical, Physical and Engineering Sciences 357(1756) (1999) 1663-1681.